Carbon molecular sieve membranes for water separation in CO$_2$ hydrogenation reactions

Document status and date:
Published: 05/07/2023

Document Version:
Publisher's PDF, also known as Version of Record (includes final page, issue and volume numbers)

Please check the document version of this publication:

• A submitted manuscript is the version of the article upon submission and before peer-review. There can be important differences between the submitted version and the official published version of record. People interested in the research are advised to contact the author for the final version of the publication, or visit the DOI to the publisher's website.
• The final author version and the galley proof are versions of the publication after peer review.
• The final published version features the final layout of the paper including the volume, issue and page numbers.

Link to publication

Carbon molecular sieve membranes for water separation in CO_2 hydrogenation reactions: Effect of the carbonization temperature

Serena Poto [a], A. Aguirre [b], F. Huigh [a], Margot Anabell Llosa-Tanco [c],
David Alfredo Pacheco-Tanaka [c], Fausto Gallucci [a,d,*], M. Fernanda Neira d'Angelo [a]

[a] *Sustainable Process Engineering, Chemical Engineering and Chemistry, Eindhoven University of Technology, De Rondom 70, 5612 AP, Eindhoven, the Netherlands*
[b] *Instituto de Desarrollo Tecnológico para la Industria Química (INTEC), Universidad Nacional del Litoral, CONICET, Güemes 3450, S3000GLN, Santa Fe, Argentina*
[c] *TECNALIA, Basque Research and Technology Alliance (BRTA), Mikeletegi Pasealekua 2, 20009, Donostia-San Sebastián, Spain*
[d] *Eindhoven Institute for Renewable Energy Systems (EIRES), Eindhoven University of Technology, PO Box 513, Eindhoven, 5600, MB, the Netherlands*

ARTICLE INFO

ABSTRACT

Carbon membranes are a potentially attractive candidate for the *in-situ* removal of water vapor in CO_2 hydrogenation reactions. Their hydrophilicity and pore structure can be tuned by properly adjusting the synthesis procedure. Herein, we assess the effect of the carbonization temperature (450–750 °C) on the performance of supported CMSM in terms of vapor/gas separation, in correlation with changes in their surface functionality and porous structure. FTIR spectra showed that the nature of the functional groups changes with the evolution of the carbonization step, leading to a gradual loss in hydrophilicity (i.e., OH stretching disappears at $T_{carb} \geq 600$ °C). The extent of water adsorption displays an optimum at T_{carb} of 500 °C, with the membrane carbonized at 650 °C being the least hydrophilic. We found that the pore size distribution strongly influences the water permeance. At all T_{carb}, adsorption-diffusion (AD) is the dominant transport mechanisms. However, as soon as ultra-micropores appear (T_{carb}: 600–700 °C) molecular sieving (MS) contributes to an increase in the water permeance, despites a loss in hydrophilicity. At $T_{carb} \geq 750$ °C, MS pores disappear, causing a drop in the water permeance. Finally, the permeance of different gases (N_2, H_2, CO, CO_2) is mostly affected by the pore size distribution, with MS being the dominant mechanism over the AD, except for CO_2. However, the extent and mechanism of gas permeation drastically change as a function of the water content in the feed, indicating that gas/vapor molecules need to compete to access the pores of the membranes.

1. Introduction

The CO_2 capture and valorization has been recognized as one of the most relevant technologies to mitigate climate change [1–4]. Most of the CO_2 utilization pathways are based on hydrogenation reactions (e.g., synthesis of methanol, DME, CO, CH_4, etc.), involving the production of large amounts of water as main by-product, thereby causing strong thermodynamic limitations and catalyst stability issues [5–7]. As a result, the removal of water from the reaction environment could enhance the catalyst and reactor performance (i.e., the conversion per pass and selectivities). The use of water-selective membranes in catalytic reactor proved to be an effective strategy for process intensification already in various reaction systems [8–17]. Since most of the CO_2 hydrogenation reactions require temperatures above 200 °C, the

membrane materials for such application must exhibit high stability in hot and humid environment. Polymeric as well as mixed matrix membranes show good performance in terms of water permeability, such that they are commonly used for waste water treatment (e.g., desalination and filtration processes) [18]. However, these membranes are not suitable for high temperature operation, especially in presence of water and CO_2 at high pressures, since they undergo swelling and plasticization phenomena, with a corresponding decay in the separation performance. On the other hand, ceramic membranes, especially zeolites, have been tested for water separation at relatively high temperature (i.e., up to 250 °C) [19]. A-type zeolites are the most common choice for application in membrane reactors for the *in-situ* removal of water [20–22]. Nevertheless, zeolite membranes suffer from very poor reproducibility, with the main challenge being the formation of a defect-free selective

layer [23,24], as well as poor long-term stability when exposed to water at relatively high temperatures [24,25].

Carbon molecular sieve membranes (CMSM) usually stand out as promising alternative, especially to polymeric membranes, given their superior separation performance (i.e., sieving effect) and to their high thermo-chemical stability [26,27]. Carbon membranes are prepared via the pyrolysis, often referred to as carbonization, of a thermoset polymeric membrane precursor at high temperature under inert atmosphere or vacuum. This process transforms a dense polymeric membrane into a porous carbon membrane which can display, at the same time, ultra-micropores (i.e., $d_p \leq 0.6$) and micropores (i.e., i.e., $0.6 \leq d_p \leq 2$). Pores in the mesopores region are considered mostly as defects in the selective layer. The ultra-micropores are responsible for the molecular sieving (MS) character of these membranes, according to which the separation of molecules is based on size-exclusion. The second important transport mechanism is adsorption-diffusion (AD), mainly occurring in micropores, which is based on the physicochemical interaction of the molecules with the pore surface [26,28]. Furthermore, when vapors are involved in the separation process, capillary condensation can also occur in the micropores of the membrane with sufficient wettability.

Thus, CMSMs are very attractive materials that can be tailor-made for a specific separation by acting on several synthesis parameters. The most common parameters are the precursor selection and the carbonization temperature/atmosphere. Phenol-formaldehyde (Novolac) resins are preferred due to their low cost and the ability to create a uniform carbon layer with only one coating step [29,30]. CMSM have been widely tested and proposed for separation of gaseous mixtures, especially for gas molecules with significantly different size and polarity, such as O_2/N_2, CO_2/CH_4, CO_2/N_2, alkane/alkene, etc [27,31–37]. Their affinity to water is well known: water adsorbs on the membrane surface already at atmospheric condition, reducing the active pore size, thus hindering the gas permeation [38]. Their potential hydrophilicity, combined with the very small kinetic diameter of water (i.e., 0.265 nm), render these membranes even more attractive for the separation of water via both vapor permeation and pervaporation processes. CMSMs have been recently proposed for dehydration of water-alcohol mixtures [39,40]. Furthermore, in our previous study, we have already demonstrated their potential for water vapor separation from (hydrogen-rich) gas mixture, which can be further improved via the integration of inorganic hydrophilic fillers (e.g., boehmite/γ-Al_2O_3) in the carbon matrix [41].

A very important and easy-to-tune parameter in the synthesis procedure of carbon membranes is the carbonization temperature (T_{carb}). Jones and Koros stated that the expansion of the gaseous products of the pyrolysis step causes a rearrangement of the polymeric structure, which corresponds to the formation of the porous system [42]. Later on, Fuertes et al. reported the gradual transformation of the porous polymer-carbon structure into dense carbon upon increasing the carbonization temperature [43]. They observed that at temperature of 600–700 °C, shrinkage of the pores occurs due to sintering, leading to the formation of ultra-micropores from the previously formed micropores. These shifts in the nature of the membrane pores led to higher permeability, as well as to lower perm-selectivity for a given separation. When the carbonization temperature is increased even further (i.e., 850–950 °C), the density of the carbon increases due to the graphitization, leading again to lower permeability and higher selectivity [44].

The effect of the carbonization temperature on the pore size distribution of Novolac-based CMSM was studied more recently by Llosa et al. [45]. They found that the membrane carbonized at 450 °C reveals a small number of pores in the range 0.4–0.9 nm, with an average pore size at 0.65 nm. Increasing the T_{carb} to 550 °C results in a larger number of pores and a pore size distribution still centered at 0.65 nm, but narrower (0.45–0.8 nm). The most significant changes occur at 600–650 °C where the number of pores increases significantly with a bi-disperse pore size distribution showing pores both in the MS and AD region. Increasing the T_{carb} even further (i.e., 700–750 °C), the porous system

starts to shrink starting from the pores in the AD region. Thus, the membrane carbonized at 750 °C displays less pores, mostly in the MS region (0.35–0.45 nm).

The carbonization temperature has also been proven to affect the hydrophilicity of the membranes. Forster et al. [46] recently reported when T_{carb} increases above 600 °C, most of the oxygen-based groups are removed, leading to a monotonic decrease of the membrane interaction with the water. However, their analysis did not cover the low carbonization temperature region, where we believe most of the changes occur. Herein, we propose a detailed study of the changes in terms of surface chemistry, hydrophilicity and pore size distribution that phenolic-formaldehyde resin CMSMs undergo with the progression of the carbonization step in the range 450–750 °C. We use FTIR analysis to identify the transformation of the functional groups of the carbon membrane, to gain insights into the pyrolysis mechanism. Thereafter, we use in-situ FTIR analysis during water adsorption/desorption steps to assess the surface interaction with water, as well as the membrane hydrophilicity, as a function of the carbonization temperature. Thermogravimetric analysis is then used to assess the membrane affinity to different type of gases (i.e., CO_2, CO and H_2). Additionally, permeation tests carried out in the range 150–250 °C with H_2O, methanol, H_2, N_2, CO_2 and CO are used to understand the interplay of the hydrophilicity and pore size distribution on the membrane performance. Thus, we aim to assess how the carbonization temperature affects the vapor/gas separation performance of CMSMs, in view of their application in membrane reactors for the in-situ removal of water.

Finally, we experimentally prove that the incorporation of CMSM in conventional packed bed reactor has great potential to enhance the synthesis of either methanol and dimethyl ether (DME) via CO_2 hydrogenation.

2. Experimental

2.1. Synthesis of the Al-CMSMs

The tubular supported Al-CMSMs were synthesized via the one-dip dry carbonization step method [45,47,48]. Tubular asymmetric α-Al_2O_3 tubes (ID: 7 mm, OD: 10 mm), with a 100 nm average pore size from Inopor® were used as support. One end of the porous α-Al_2O_3 was connected to a dense alumina tube using a glass sealant. The other end was closed with the same sealant to obtain a dead-end membrane. The open end was then connected to a standard Swagelok component to collect the permeate flow. The support were dip-coated by means of a vacuum pump in a solution with: 13 wt% of Novolac resin, 0.6 wt% of ethylenediamine, 2.4 wt% of formaldehyde, 0.8 wt% of 10 wt% aqueous dispersion of boehmite nanosheets with a particle size of 8–20 nm (*Alumisol* provided by Kawaken fine Chemicals) [48] and *N*-methyl-2-pyrrolidone (NMP) as solvent. The Al-CMSM membranes were dried at 90 °C and carbonized in a temperature range from 450 to 750 °C, following the procedure reported in our previous study [41]. The remaining precursor solution was used to prepare unsupported membrane films carbonized at different temperatures, as the Al-CMSMs, with the same procedure used for the supported membranes.

2.2. FTIR analysis

The CMSM surface of as prepared and treated samples was study by DRIFT spectroscopy to identify main functional groups which are relevant for the permeation. The adsorption of water was studied using a Harrick DRIFT cell. Time-resolved infrared spectra (up to 1 spectrum/ 0.39 s) were recorded at a resolution of 4 cm^{-1} using an FTIR spectrometer (Thermo iS50 with a cryogenic MCT detector). The CO_2 and water vapor contributions from the atmosphere to the spectra were eliminated by purging continuously with purified air (Parker Balston FTIR purge gas generator) on the bench of the spectrometer and the optical path. The gas flow was regulated using mass flow meters (Cole-

Parmer). The entrance of the gases was controlled by a flow-through 10-ways valve electronically actuated (Vici-Valco) synchronized with the FTIR. The gas composition at the exit of the cell was analyzed by mass spectrometry (Prisma QMG220, Pfeiffer). Water (2%) in He was obtained from a gas saturator filled with pure water immerse into a thermostatic bath.

The cell was filled with 50 mg of unsupported carbon membrane sample. Before the experiments, the sample was treated by flowing/He (300 °C, 1 h, 5 °C/min), and then cool down to 30 °C. The adsorption of water (2%)/He (50 mL/min) was performed at 30 °C. Next, the desorption of water was studied by changing from 2% water to pure He. After the adsorption/desorption experiments, the samples were heated to 300 °C (5 °C/min).

2.3. Thermogravimetric analysis

The adsorption of gases (CO_2, H_2 and CO) by the membrane was studied via thermogravimetric analysis (TGA). The TGA setup (Fig. 1) consists of a microbalance (MK2-5 M from CI-Precision) with a sensitivity of 1 µg. The balance (M) is kept at a constant temperature and in an inert atmosphere (i.e., N_2 is fed at 0.5 L/min via FC101) to prevent any contamination from reactive gases. The balance is attached via a platinum wire to a porous Al_2O_3 basket (0.5 cm d x 1.5 cm l) in which the solid sample can be loaded. The basket is then placed in a ceramic tube (ID 15 mm) which is then surrounded by a stainless-steel vessel and heated via an electric oven. The oven is controlled via thermocouple placed in the proximity of the basket, to guarantee a stable and isothermal operation. The relevant gases are fed from gas cylinders by means of mass flow controllers (FC), while pressure is regulated using a back pressure regulator (BPC) from Bronkhorst. To conduct the analysis ca. 40 mg of unsupported carbon membrane sample were loaded into the

basket and placed in the TGA system. Prior to any analysis, a pretreatment was carried out to remove any adsorbed water from the atmosphere: the sample was heated up to 300 °C at ambient pressure, under a N_2 flow of 0.5 L/min and kept at these conditions for 1 h [49] (note that the CMSMs are inert with regard to N_2, see S.I. for more details). After the pre-treatment, the system was cooled down to the desired temperature (i.e., 200 °C) under N_2 flow. Afterwards, the analysis gas was fed at flow rate of 0.5 L/min and the pressure was increased progressively up to 10 bar. An equilibration time of 40 min at each pressure point was guaranteed to allow the sample to achieve stable weight due to the adsorption phenomena. Blank tests were carried out with the empty basket using the same procedure described above, to correct for the buoyance forces exerted by the feeding gases on the basket. During the analysis the weight of the sample and basket was recorded every 5s. However, only steady state values (w_{ss}) were used to determine the weight variation (Δw) related to the adsorption phenomena, as reported in Eqs. (1) and (2).

$$\Delta w = w_{ss} - w_0 \tag{1}$$

$$\Delta w_{corrected} = \frac{\Delta w_{sample} - \Delta w_{blank}}{w_{sample,0}} \bullet 100 \% \tag{2}$$

Where w_0 is the initial weight of either the sample (after pre-treatment) or the empty basket and $\Delta w_{corrected}$ is the net percentage weight increase of the sample due to the adsorption of gases.

2.4. Permeation experiments

The permeation experiments were carried out in a dedicated setup, which was described in our previous study [41], along with the adopted experimental procedure. All the permeation experiments were carried
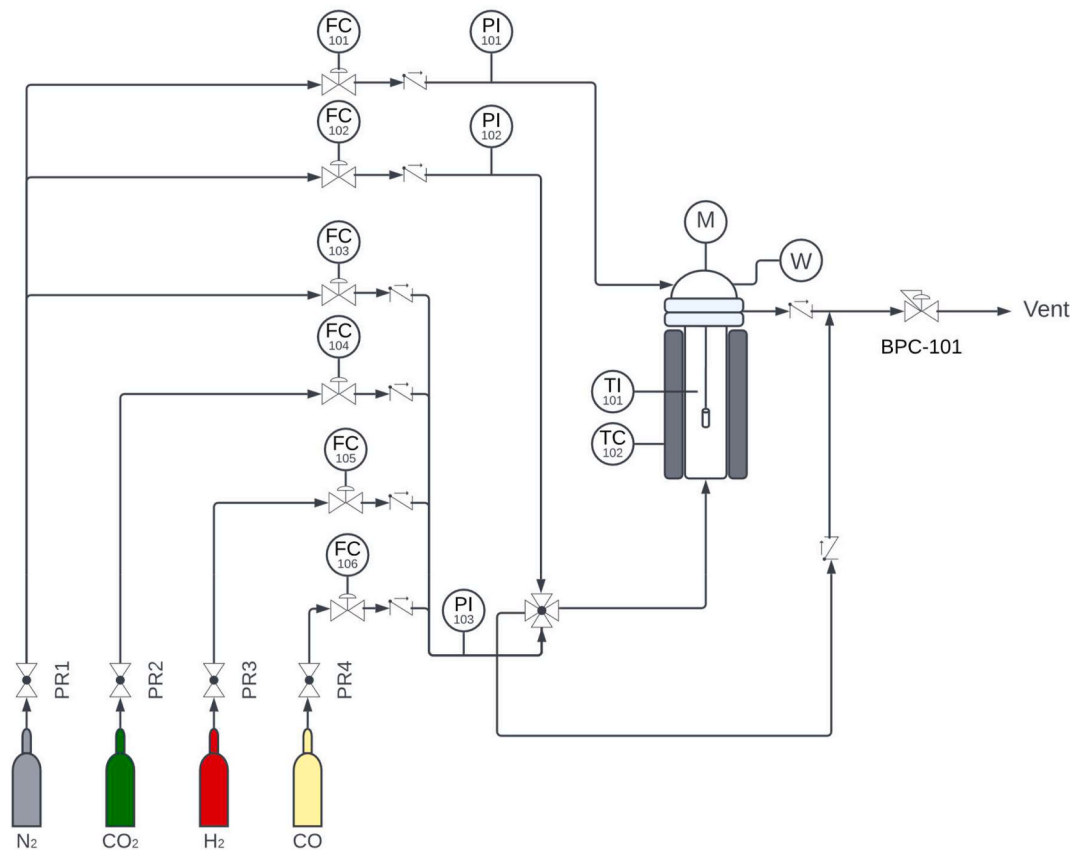

Fig. 1. Schematic representation of the TGA setup, where FC, PI, TI, TC indicates mass flow controller, pressure meters, temperature indicators and temperature controllers, respectively. BPC represents the back pressure regulator, M the micro-scale and W the weight indicator.

out at a temperature of 150–250 °C, a pressure gradient across the membrane (ΔP) of 3 bar and a total feed flow of 1 L·min^{-1}. To derive the water and methanol permeance, the membrane was exposed to a flux of either water or methanol, containing 7.5 vol% of N_2, as required by the Controlled Evaporator Mixer (C.E.M.). After 40 min (i.e., steady state), the N_2 permeated flow was measured, and the water/methanol was collected and weighted from both the retentate and the permeate side. The vapor – water or methanol – permeance was calculated as follows:

$$\wp_{i,vapor} = \frac{W_{i,permeated} \bullet M_{w,i}^{-1}}{\Delta t \bullet \Delta P_i \bullet A_m} \tag{3}$$

Where $w_{i,permeated}$ is the weight of the water/methanol collected from the permeate, $M_{w,i}$ is its molecular weight, Δt is the time span of the permeation experiment, A_m is the membrane area and ΔP_i is the gradient in partial pressure across the membrane, which accounts also for the presence of N_2 in the feed.

The permeance of the gases (i.e., N_2, CO_2, H_2 and CO) was measured in three different conditions: 1) through a humid membrane; 2) through a dry membrane; 3) exposing the membrane to a binary mixture of water and each gas. In the first case, a pure gas flow was fed to the membrane which was prior exposed to water vapor at the same temperature and pressure of the permeation experiment. In the second case, the membrane was first dried overnight at 250 °C under N_2 flow to remove all the adsorbed water and then exposed to a pure gas flow. In the third case, an equimolar mixture of water vapor and one of the gases of interest was fed to the membrane, with a total feed flow of 1 L·min^{-1}. After 40 min, as in the vapor permeation tests, the gas permeated flow was measured and the water was condensed, collected and weighted from both the permeate and retentate side. In all three cases, the gas permeance was calculated as follows:

$$\wp_{i,gas} = \frac{\Phi_{i,perm} \bullet V_m^{-1}}{\Delta P_i \bullet A_m} \tag{4}$$

Where $\Phi_{i,perm}$ is the volumetric flow rate of the permeated gas and V_m is the gas standard molar volume.

2.5. Activation energy calculation

Adsorption-diffusion and molecular sieving are activated phenomena. As such, they show an exponential dependence with temperature, which is regulated by an activation energy. The permeance due to these mechanisms is commonly described by an Arrhenius-type equation, as shown in Eq. (5).

$$\wp_i = \frac{\Delta P_i}{RT} D_i^0 \, exp \left[\frac{-(E_{act,i} - E_{ads,i})}{RT} \right] \tag{5}$$

Where D_i^0 is the diffusion coefficient, $E_{act,i}$ is the activation energy of either molecular sieving or adsorption diffusion, and $E_{ads,i}$ is the energy of adsorption. This equation is used to identify and describe the prevailing transport mechanism, looking at the trend of the permeation flux as a function of temperature. In case of molecular sieving, the activation energy for the gas to diffuse into the ultra-micropores is always higher than its adsorption energy, thus leading to an overall activation energy which is positive ($E_{act,MS,i} - E_{ads,i} > 0$). As a result, transport due to molecular sieving is enhanced for increasing temperature. Conversely, the difference in activation and adsorption energy for adsorption-diffusion can be either negative or positive. For gases with high adsorption energy, $E_{act,AD,i} - E_{ads,i} < 0$, meaning that an increase in temperature will result in a decrease in the permeation flux. On the contrary, if the activation energy is lower than the energy for the adsorption-diffusion, the overall term will become positive and an increase in temperature will result in an increase in the permeation flux, as with the molecular sieving [50]. We will refer at the difference ($E_{act,i} - E_{ads,i}$) as apparent activation energy ($E_{act,i}^{app}$), which is a parameter

that can be determined fitting the permeance data as a function of the operating temperature.

2.6. Packed bed membrane reactor tests

To demonstrate that the Al-CMSMs developed in this work present a highly attractive alternative to zeolite and ceramic membranes for their application for the in-situ removal of water during CO_2 hydrogenation reactions, we tested a carbon membrane ($T_{carb} = 600$ °C) under reactive conditions for the production of methanol and dimethyl ether (DME).

The experimental setup used for these experiments is described in our previous work [51], where the reactor was replaced with a stainless-steel vessel (OD 28.5 mm, L 150 mm) with a top flange for the connection of the membrane tube. Both a sweep gas and a permeate line are connected to the inner side of the membrane via the top flange. The catalyst bed is placed in the outer space. To properly compare the two reactor technologies under the same conditions, the packed bed reactor (PBR) experiments were repeated replacing the membrane with a stainless steel tube having the same size. For the methanol production we used a Cu/ZnO/Al$_2$O$_3$ catalyst, which was then physically combined with a HZSM-5 for the one-step DME synthesis. More details on the experimental procedure are reported in a separate publication [52].

3. Results and discussion

3.1. Insights into the carbonization mechanism and the effect of the carbonization temperature on the CMSM surface chemistry

The FTIR spectra of the as prepared CMSM samples obtained after thermal treatment (i.e., removal of the adsorbed water) is reported in Fig. 2. All the peaks, together with their assignation, are resumed in Table 1.

In the region 3700-3100 cm^{-1}, the OH stretching signals (ν(OH)) for the samples carbonized at 450, 500 and 550 °C are observed. The samples treated at 600 °C and higher temperatures do not show any signal in this band, which is in agreement with literature [53] (see integrated OH bands in Fig. 3a). Indeed, Morterra et al. reported that for temperatures above 550 °C, the resin undergoes drastic changes. In this band, we can identify three main peaks: 1) a shoulder at 3650 cm^{-1} which corresponds to free or unbridged OH groups [54], 2) a stronger peak at 3545 cm^{-1} that corresponds to the bridged OH groups from the phenols of the Novolac resin [53,55,56] and 3) a strong and broad polymeric OH peak at 3450 cm^{-1} that is ascribed to the intense intra-molecular OH–OH interactions [53,54]. When comparing the area of the bridged and free OH band with those of the bridged and polymeric band, via the integrated OH$_{3550}$/OH$_{3650}$ and OH$_{3550}$/OH$_{3450}$ (Fig. 3b) ratios, respectively, it is clear that increasing the carbonization temperature from 450 to 550 °C causes polymer branching via condensation reactions of the OH groups of the phenol rings, forming diphenyl ethers (Eq. 6).

As a result, we lose some of the bridged OH groups of the phenols due to the formation of the ether linkage. At the same time, this reaction could lead to the formation of more free OH (i.e., water produced via condensation), which explains the faster decrease in the ratio OH$_{3550}$/OH$_{3650}$. Furthermore, the condensation reaction seems to influence the intra-molecular interaction between the remaining phenol groups to a lesser extent, evidenced by the little influence of carbonization temperature on the OH$_{3550}$/OH$_{3450}$ ratio. This could also indicate an increase in crosslinking via intra-molecular interaction [56].

In the region 3100-2700 cm^{-1} we can observe the CH stretching vibration (ν(CH)). First, the sample carbonized at 450 °C displays two clear aromatic CH bands at 3047 and 3025 cm^{-1}. With the increase in the pyrolysis temperature, the first band shifts to higher wavenumbers (i.e., 3055 for the sample carbonized at 600–650 °C), and the intensity of both bands gradually decreases to medium (600 °C) and weak (650 °C), to completely disappear for temperatures above 650 °C. However, the
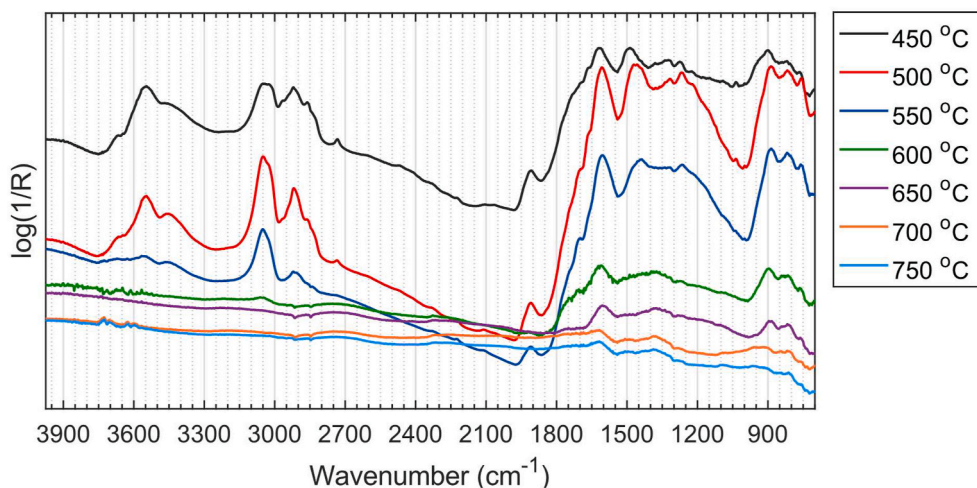
Fig. 2. FTIR spectra of the as prepared CMSM samples after thermal treatment.

aliphatic CH bands, typically found in the region below 3000 cm^{-1}, disappear first. In the aliphatic region, we can identify the CH$_3$, CH$_2$ and aldehyde (C=OH) stretching. The CH$_3$ stretching bands (2920 and 2860 cm^{-1}) corresponding to the ν_{as}(CH)) lose their intensity with the carbonization temperature. As a matter of fact, Trick et al. [56] proved that the aliphatic bands first increase and then decrease with the progression of the pyrolysis reactions. This is linked to the transformation that the resin undergoes especially in the region 500–520 °C, where Morterra et al. suggests the scheme reported in Eq. 7 [53]. However, all the bands related to the aliphatic CH groups completely disappear at 600 °C, which is in agreement with literature [53].

The relative signal intensity and position change with the pyrolysis temperature. Fig. 4 shows the CH$_{alkyl}$/CH$_{aromatic}$ ratio as function of the carbonization temperature, from which is clear that the relative amount of alkyl CH decreases with temperature much faster than the aromatic bands. At temperatures above 650 °C, no CH stretching vibrations are observed.

An additional signal is observed at 2730 cm^{-1} for temperatures below 550 °C. This signal can be assigned to the ν(CH) of aldehyde-like species [[R–C=O)–H] [57].

The region between 2000 and 1000 cm^{-1} corresponds to the fingerprint region of our material, where a series of intense, overlapped and broad bands are observed. The peak at 1705 cm^{-1} corresponds to the stretching of the carbonyl group ν(C=O). The base location of this peak is 1720 cm^{-1}, but the presence of benzene rings in the surrounding molecular structure increases the dipolar character of the C=O, leading to a shift of ca. 20 cm^{-1} towards lower wavenumbers [56]. The ν(C=O) is not observed for temperature higher than 600 °C.

The C–C stretching of aromatic rings are observed at ca. 1600, 1585 and 1450 cm^{-1}. The signal at 1910 cm^{-1} could correspond to overtones and/or combination bands of the aromatic rings [57]. These peaks decrease its intensity at higher carbonization temperatures. On the other hand, the CH deformation (δ(CH)) of aliphatic bridges CH$_3$ and CH$_2$ are observed at 1485 and 1400 cm^{-1}. A shift in the peak position, as well as a change in weaker adjacent peaks are indications of changes in the nature of the aliphatic bridges [56].

The region 1300-1200 cm^{-1} is assigned to the stretching of the C–O bond (ν(CO)). In particular, two signals at 1270 and 1225 cm^{-1} are observed, which indicate the C–O stretching of the diphenyl ether structure, formed via condensation reaction of two phenol groups (scheme of Eq. REF Eq6 \h 6), and of the phenol group, respectively. These signals are absent for the samples carbonized at temperatures higher than 650 °C.

For all the signals in the fingerprint region, their intensity increase with pyrolysis temperature from 450 to 500 °C and then decrease. At

temperatures higher than 650 °C only a broad signal at 1350 cm^{-1} remains, which is also indicative of the δ(CH) of aliphatic bridges.

Finally, signals in the range of 1200-1000 represents bending of the OH group (δ(OH)), which are only visible for the sample carbonized at 450 °C, in line with what we observed with the OH stretching ν(OH)

The range below 1000 cm^{-1} is usually attributed to the deformation of the CH bond (δ(CH)) of aromatics. Changes in the relative heights of these peaks indicate ring substitution reactions, in line with what found in literature [56]. The shift from lower (760 cm^{-1}) to higher (890 cm^{-1}) wavenumber, represent an increase in the ring substitution related to the increase in carbonization temperature (Fig. 5), which overall leads to a decrease in H free atoms (i.e., OH and alkyl groups substitution).

All the peaks, together with their assignation, are summarized in Table 1.

The evolution of the bands is in agreement with the study of Trick et al. [56] via the analysis of the gas evolution. To summarize, we can identify four main steps in the carbonization.

- *Step 1*: crosslinking of the cured resin (R) via the formation of the CH and O (ether) links (R$_{CH}$ and R$_O$, respectively), as described via Eq. 7 and Eq. 6, respectively. This step leads to a loss in C–OH and alkyl groups.
- *Step 2*: stripping of the previously formed CH crosslinks, as well as of the methylene crosslinks from the original cured resin. The aliphatic CH concentration decreases with respect to the ring-related CH bonds. This step leads to the formation of C-crosslinked char (Ch$_C$).
- *Step 3*: reaction with gaseous products leads to the formation of direct aromatic-aromatic link (Ch$_{Ar}$).
- *Step 4*: splitting of the H atoms directly bonded to the benzene nuclei, to form the final char structure (Ch) with coalesced rings.

The evolution of the char structure as described in step 2, 3 and 4 is sketched in Fig. 6.

The Novolac-based dipping solution used in this study for the preparation of the carbon membranes includes two additives: 0.6 wt% of ethylenediamine (C$_2$H$_8$N$_2$) and 0.8 wt% of 10% aqueous dispersion of boehmite nanosheets. The NH stretching vibrations occur in the same range of the OH vibrations, but they are usually much weaker. Primary amines show some deformation peaks related to the NH$_2$ bond at ca. 1650 cm^{-1}, which we did not detect. On the other hand, secondary amines (R–NH–R') show deformation vibration at ca. 1600 cm^{-1}, which would overlap with the aromatic C=C stretching. However, we should keep in mind that the nitrogen content found in the carbonized samples via elemental analysis (see SI) is ca. 1–1.5 wt%, which indicates that any

Table 1
Overview of peak identification of the FTIR samples of the as-prepared CMSM samples carbonized at various temperatures (s = strong, m = medium, w = weak and vw = very weak signal).

T_{carb} (°C)	$\nu(OH)$	$\nu(CH)$ aromatic	$\nu_{as}(CH)$.	$\nu_s(CH)$	$\nu(CH)$ aldehyde	$\nu(C=O)$
450	3650 m 3545 s 3440 s, b	3047 s 3025 s	2920 s 2860 s	2900 m 2825 m 2730 w	2730	1705 s
500	3650 s 3545 s 3450 s, b	3050 s 3025 s	2918 s 2855 s	2900 m 2820 m 2735 w	2735	1705 s
550	3650 s 3545 s 3450 s, b	3050 s 3025 s	2918 s 2855 s	2900 m 2820 w 2735 vw	2735	1705 s
600	–	3055 m 3025 m	–	–	–	1705 s
650	–	–	–	–	–	–
700	–	–	–	–	–	–
750	–	–	2958 w 2927 w 2855 w	–	–	–

Tetra-substituted benzene ring	$\nu(C–C)$ aromatic	$\nu(C–C)$ aromatic and $\delta(CH)$ of CH_2 and CH_3	$\nu(CO)$ diphenyl ether structure	$\delta(OH)$	Benzene ring substitution
1700–1730 m	1616 s 1585 m	1485 s 1440 s	1300-1200 s (1270 & 1225)	1200–1000	888 s, 823 s, 760 s
1700–1730 m	1605 s 1585 m	1460 s1430 s	1300-1200 s (1270 & 1225)	–	883 s, 820 s, 754 s
1700–1730 m	1605 s 1585 m	1442 1430 s	1300-1200 s (1270 & 1225)	–	880 s, 820 s, 756 s
1700–1730 m	1624 s 1585 m	1440 w 1400-1300 w	1270 m	–	893 m, 820 w, 760 w
–	1600 s 1585 m	1440 w 1400-1300 m	1270 m	–	885 m, 820 w, 760 w
–	1600 m 1585 w	1400-1350 w	–	–	900 w
–	1600 m 1585 w	1400-1350 w	–	–	905 w

peak related to this element is in general less significant (i.e., comparable to the noise of the measurement) than the peaks related to the C, H and O bonds. As a result, we believe that the N-related bonds do not contribute much to the FTIR spectra of our samples.

Furthermore, in a previous work [41], we proved the absence of any Al–C interaction, therefore, boehmite contributes to the FTIR spectra in the free OH bands, although, likewise the N-bonds, this contribution is very little when compared to the bands linked to the carbon skeleton of the resin.

Analysis of the FTIR spectra with the carbonization temperature in a wider range (450–750 °C) shows that the pyrolysis process does not necessarily leads to a drastic shift from hydrophilic to hydrophobic behavior. The resin undergoes drastic changes in the range 450–550 °C, where functional groups transformation occurs prior to their disappearance (i.e., formation of char structures). Therefore, the functional groups formed in this range could be either less or more hydrophilic than the ones from the original cured resin. However, we expect that above 600–650 °C the hydrophilicity is gradually lost, as reported elsewhere [58]. The affinity of the samples carbonized at different temperatures to water will be addressed in the following section.

3.2. Water adsorption/desorption on the CMSM surface studied via in-situ FTIR

The membrane carbonized at 500 °C is used as example to qualitatively analyze the evolution of the FTIR spectra with time during the water adsorption (Fig. 7a) and desorption step (Fig. 7b). When the membrane sample is exposed to 2 vol% water, the FTIR signal displays a development and subsequent increase of intensity of peaks in the band region of the OH stretching, and to a milder extent, of the OH bending (see S.I.). In particular, in the OH stretching region, we can identify 4 peaks [59]: the peaks at ca. 2990 cm^{-1}, 3320 cm^{-1} and 3490 cm^{-1}, all representing the monolayer water adsorbed to the hydrophilic pores via the formation of strong, medium-strong and weak H-bonds, respectively. The peak at ca. 3560 cm^{-1} can be ascribed to the free or unassociated water, which means isolated water molecules that are either physically adsorbed onto the membrane surface or interacting with the strongly adsorbed water. Fig. 7a shows that after ca. 30 min, the system achieves a steady state condition and the FTIR spectra stabilize. However, when the water is removed and the sample is only exposed to a He environment at the same temperature and pressure (i.e., 30 °C and ambient pressure) – Fig. 7b – the membrane surface cannot restore its initial (dry) status, as reported in Fig. 2, even when achieving steady state condition. Indeed, some water is still bonded to the membrane surface. This indicates that the water adsorption/desorption phenomena displays a hysteresis behavior. To restore the initial status of the membrane surface, the membrane needs to be exposed to an inert atmosphere (i.e., N_2) at 300 °C for 1 h.

The high intensity peaks (i.e., in the region 3700-3100 cm^{-1}) characterizing both the water adsorption and desorption spectra were integrated and normalized with the maximum integrated band intensity (i.e., steady state), as shown in Fig. 8a and b, respectively. During the water adsorption, all the peaks achieve a steady state condition with the same rate. However, during the desorption step, only the free water molecules completely desorb and at a higher rate. On the other hand, the water molecules bonded to the membrane surface via H-bonds do not desorb completely, showing a residual peak area which is larger for the medium-strong than for the weak H-bonds. Therefore, the water directly adsorbed onto the membrane pores (i.e., via H-bonds) appears to be responsible for the hysteresis behavior.

The same water adsorption/desorption experiment was carried out on all the membrane samples carbonized at different temperatures (i.e., 450–750 °C). Fig. 9 displays the FTIR spectra obtained after subtracting the spectra of the dry membrane (Fig. 2) from the steady state water adsorption spectra. For the samples carbonized at temperatures higher than 550 °C, the signal is much weaker and the peaks corresponding to strongly adsorbed water via medium and strong H-bonds disappear (i.e., peaks at lower wavenumber), while the peak representing mainly weak bonded or free water is much broader. At 600 °C and 650 °C, the membrane surface loses the hydroxyl and carbonyl groups, respectively, which are the most polar functional groups able to form hydrogen bonds with water.

Analyzing the low carbonization temperature region (i.e., 450–550 °C), we observe that the sample carbonized at 500 °C adsorbs the highest amount of water, followed by the sample carbonized at 550 and 450 °C. We believe that the higher hydrophilicity of the 500 ºC-carbonized sample is linked to the C–O, C=O, aromatic and aliphatic CH groups (corresponding to the signals in the region 2000 and 1000 cm^{-1} that display a peak at 500 °C), which all increase the probability of the water to adsorb onto the membrane surface.
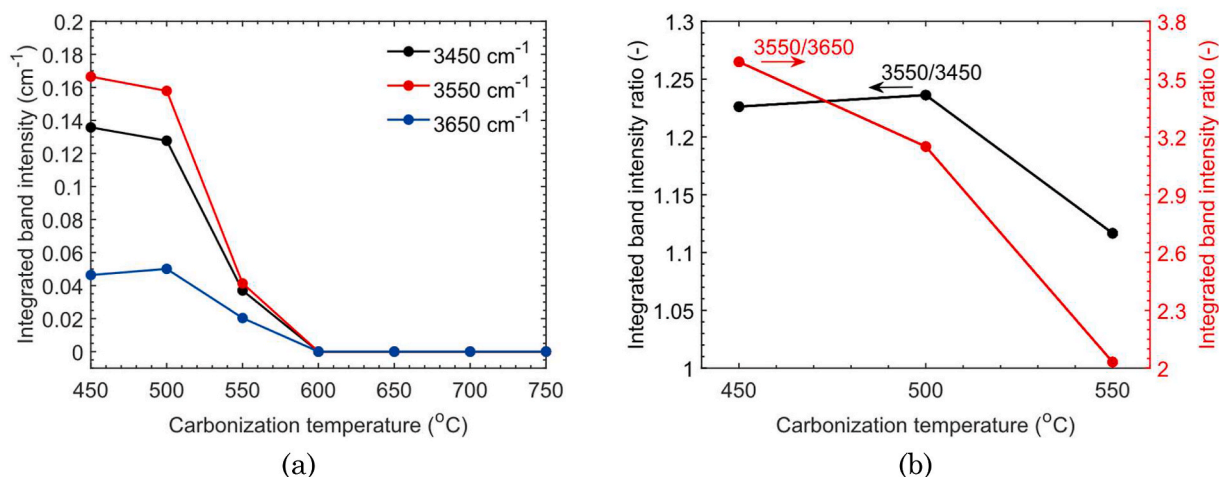
Fig. 3. Integrated OH_{3450}, OH_{3550} and OH_{3650} (a) and OH_{3550}/OH_{3650} and OH_{3550}/OH_{3450} integrated bands ratio (b) as a function of the carbonization temperature, derived from the spectra in Fig. 2.
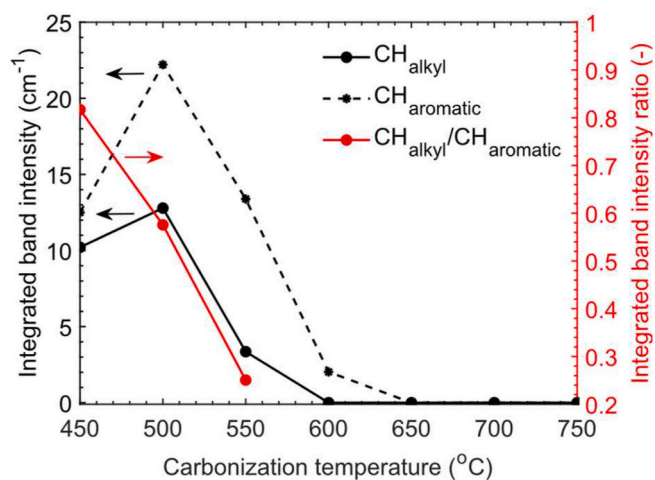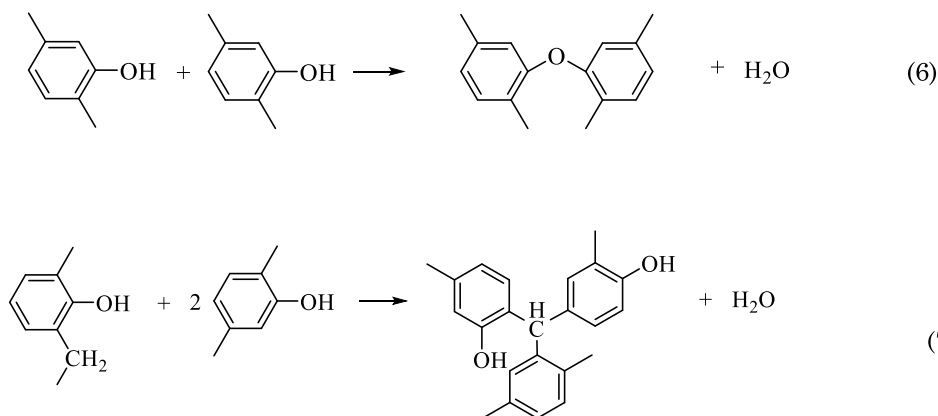

$$(6)$$

$$(7)$$

Fig. 4. Integrated CH_{alkyl} and $CH_{aromatic}$ bands on the left and $CH_{alkyl}/CH_{aromatic}$ integrated band ratio as a function of the carbonization temperature, derived from the spectra in Fig. 2.

Fig. 5. Integrated CH_{890}/CH_{760} band ratio (indication of ring substitution) as a function of the carbonization temperature, derived from the spectra in Fig. 2.

When zooming into the high carbonization temperature region (see S.I.), we observe that the signal is quite weak and noisy. However, it is clear that the hydrophilicity tendentially decreases for $T_{carb} \geq 600\ °C$.
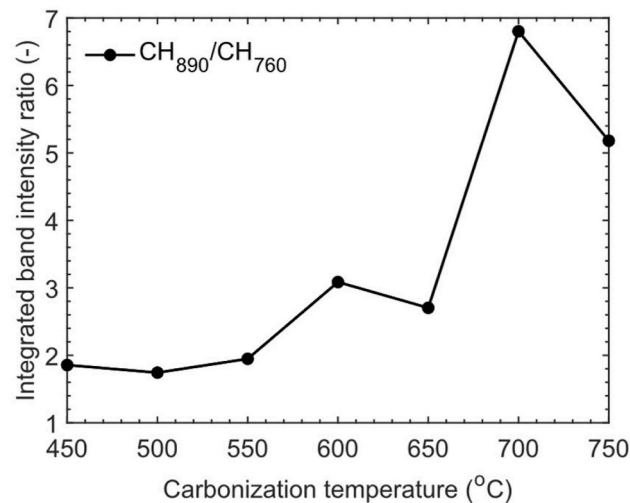
3.3. Gas adsorption properties derived via thermogravimetric analysis

To assess whether the adsorption diffusion is a relevant transport mechanism for gas permeation, the affinity of the membranes
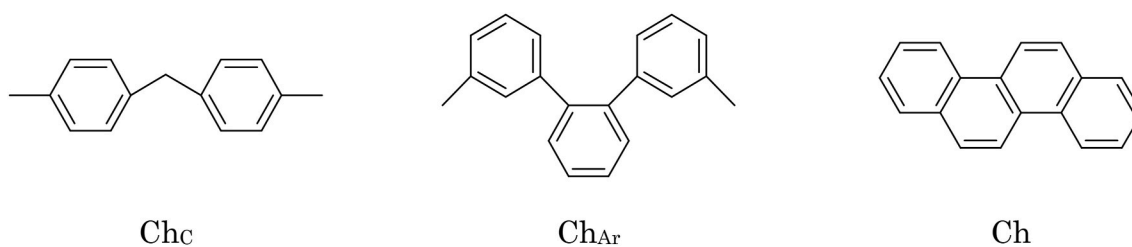
Fig. 6. Evolution of the structure of the char from carbon crosslink (Ch$_C$) to aromatic crosslink (Ch$_{Ar}$) and to coalesced rings (Ch).
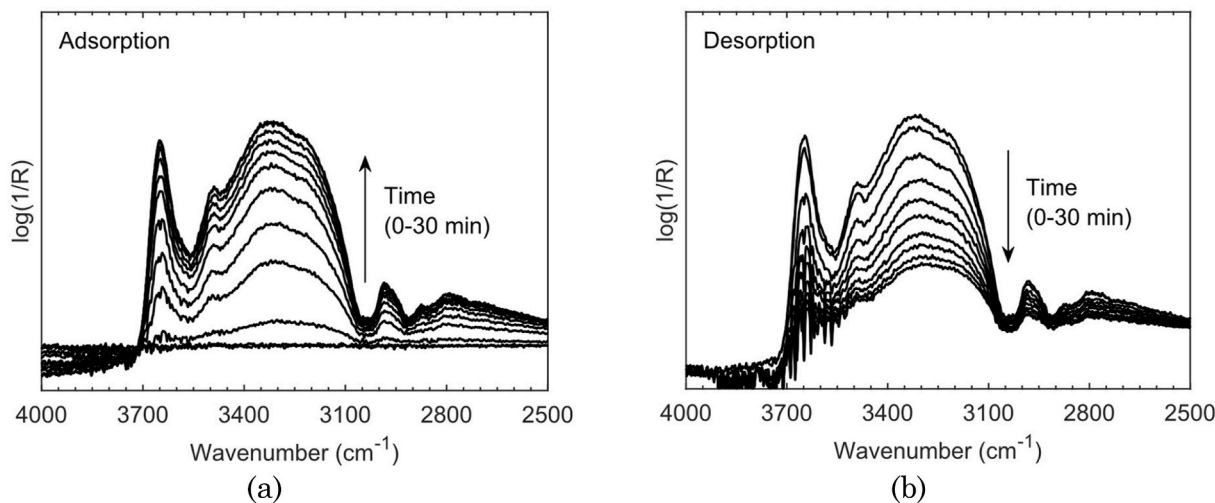

Fig. 7. FTIR spectra obtained when exposing the membrane carbonized at 500 °C to a 2 vol% water/He environment (a – water adsorption) and to a He environment (b – water desorption) at 30 °C and ambient pressure, as a function of time.
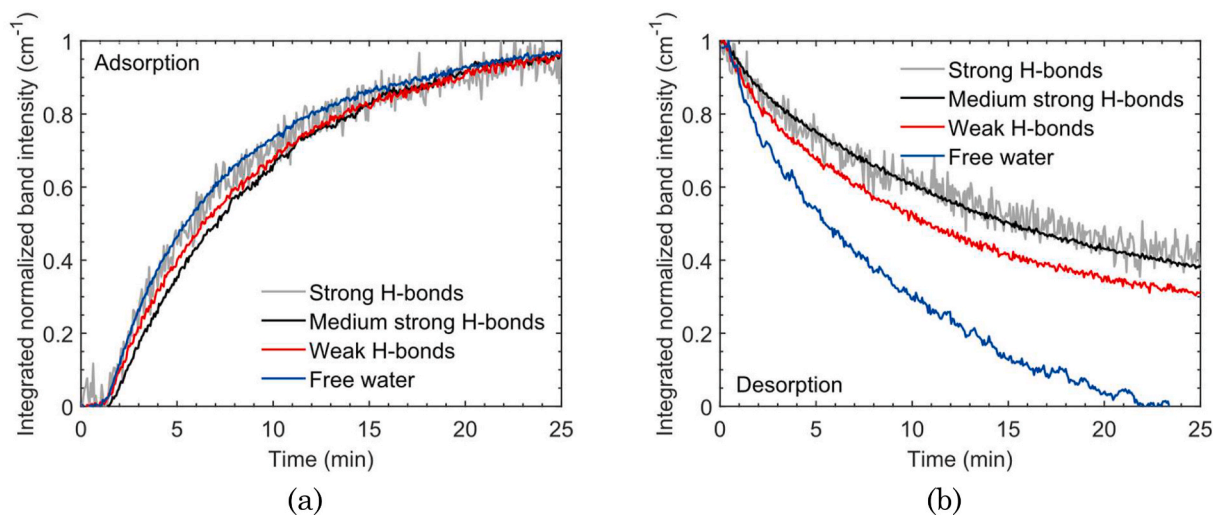

Fig. 8. Integrated normalized band intensity corresponding to the strong H-bonds (2990 cm^{-1}), medium strong H-bonds (3320 cm^{-1}), weak H-bonds (3490 cm^{-1}) and to the free water (3560 cm^{-1}) as a function of time during the water adsorption (a) and desorption (b) step, obtained from the FTIR spectra of Fig. 7 (membrane sample carbonized at 500 °C).

carbonized at different temperatures to the gas of interests (i.e., CO$_2$, H$_2$ and CO) was studied via thermogravimetric analysis (TGA). As shown in the previous section, the membrane carbonized at 500 °C displays the highest adsorption capacity for water vapor, being the pores walls rich in functional groups. Therefore, this membrane sample was used again as a reference for further studies. We found that the adsorption of CO and H$_2$ at temperatures relevant to the permeation (i.e., 200 °C) can be neglected, at least in the pressure range of 1–10 bar. The only gas

showing affinity to the membrane surface is CO$_2$, as anticipated in our previous study. Therefore, the CO$_2$ adsorption was systematically studied for all the membrane samples. For all membranes, the amount of CO$_2$ adsorbed increases as a function of pressure, following a Dubinin-Astakhov type of isotherm, as reported elsewhere [49]. Furthermore, Fig. 10 shows that the weight variation associated to the CO$_2$ adsorption generally increases with the carbonization temperature, with the membrane carbonized at 650 °C being the only one out of the trend.
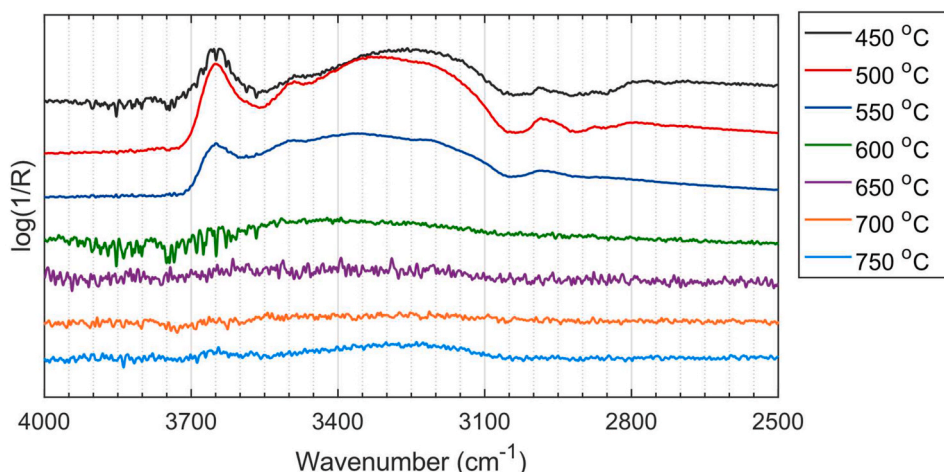
Fig. 9. FTIR spectra of the carbon membrane samples carbonized at different temperatures, obtained after subtraction of the characteristic dry membrane spectra (Fig. 2) from the steady state spectra obtained when exposing each membrane sample to a 2 vol% water/He environment at 30 °C and ambient pressure (water adsorption experiment).
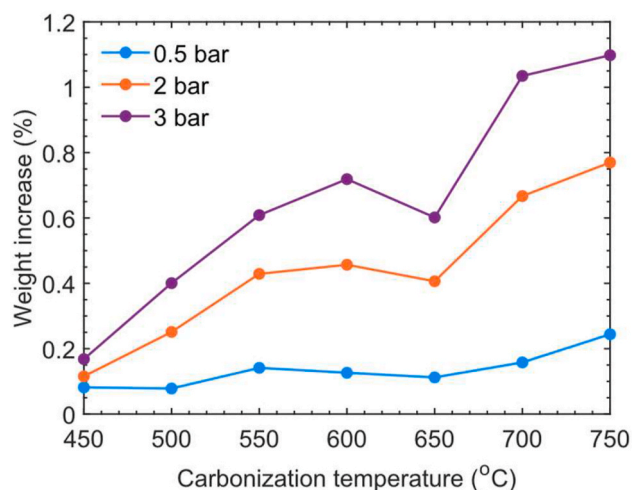

Fig. 10. Weight increase (%) recorded during the CO_2 TGA test at 200 °C as a function of the carbonization temperature for three values of pressure (0.5, 2 and 3 barg).

Indeed, the sample carbonized at 650 °C displays a lower adsorption capacity than those carbonized at 600 and 700–750 °C, in agreement with what found with the water adsorption (section 3.2). This finding implies that although no noteworthy differences can be observed in the FTIR spectrum among the carbonized membranes produced at temperatures of 600 °C and 700–750 °C, when compared to the membrane obtained at 650 °C, the latter displays a lower surface area. This reduction results in fewer functional groups being available to expose to the gaseous atmosphere for the adsorption of CO_2.

The increase in the CO_2 adsorption with the carbonization temperature can be ascribed to two reasons: the change in the surface chemistry and 2) the change in the surface area with the carbonization temperature. The surface functionality of the membranes was studied via FTIR, where no bands related to N-containing group were detected, due to the very little concentration (i.e., 0.6 wt%) of the of ethylenediamine ($C_2H_8N_2$) in the Novolac-based dipping solution that was used for the preparation of the membranes. On the other hand, we cannot exclude any transformation of the amine group involving the incorporation of the nitrogen atom in the aromatic ring, leading to the formation of pyridine/pyridone structures within the pyrolysis process. L. Geunsik et al. [60] proved via DFT calculation that the binding energy of CO_2 to pyridine/pyridone groups is stronger than for amine groups, which could explain the increase in the CO_2 uptake with the carbonization temperature. Secondly, the porous structure (i.e., pore size, pore size distribution and surface area) of these membranes, has been proven to be affected by the carbonization temperature [45,47]. As reported in Section 1, the membrane carbonized at 450 °C has few pores, mostly in the range 0.4–0.9 nm. Thus, at 450 °C the membrane has a small pore volume, combined with relatively large pores, which also translate into a small surface area. At intermediate T_{carb} (600–650 °C), the membranes display a bimodal distribution, with MS and AD pores. These membranes are expected to have the largest surface area. Finally at higher T_{carb}, the porous system shrinks, leaving most of the pores in the MS region. As a result, the surface area of the membranes is expected to display an optimum with the carbonization temperature, which is something that does not reoccur in the CO_2 uptake (Fig. 10). Thus, the results suggest that at low carbonization temperature, the increase in the CO_2 adsorption is linked to the increase in the surface area with the carbonization temperature. At higher T_{carb}, despites the shrinkage of the porous structure, the CO_2 adsorption continue to increase due to the transformation of the amine group into the pyridine/pyridone structure, due to the pyrolysis process. This theory agrees with the lower CO_2 adsorption capacity found at 650 °C, where the effect of the surface area prevails on the surface chemistry.

Water adsorption tests via thermogravimetric analysis were not carried out due to setup limitations. However, the water adsorption was studied at low temperature and pressure (i.e., 30 °C, 2 vol% water in He and ambient pressure) via in-situ FTIR analysis (section 3.2). The same type of experiment was repeated replacing water by CO_2. No signal due to the CO_2 adsorption was detected, as CO_2 seems to require higher pressures to adsorb onto the membrane surface. Thus, although we could not quantify the water adsorption at conditions relevant for the permeation (i.e., 200 °C), we expect that it would be even more relevant than the CO_2 adsorption. This is also confirmed by the characteristic functional groups of the surface of the membranes (section 3.1), which interact more with water than CO_2.

3.4. Permeation properties of the supported Al-CMSMs

This section focuses on the permeation properties of the tubular supported Al-CMSM. First, we assess the effect of the carbonization temperature through the analysis of the single vapor (water and methanol) and single gas permeance through humidified membranes. Then, gas and gas/vapor permeation through both a humid and a dry membrane will be discussed in order to elucidate the permeation mechanism.

3.4.1. Effect of the carbonization temperature on the vapor/gas permeation properties

Fig. 11a shows that the permeance of N_2 ($\wp_{N_2}$), CO ($\wp_{CO}$) and H_2 ($\wp_{H_2}$) measured at 200 °C, first increases with the carbonization temperature, displaying an optimum in the region 600–700 °C, to decrease again at 750 °C. The same trend repeats at all the operating temperatures in the range 150–250 °C (see SI). In the optimum region, two peaks are identified: one at 600 °C and one at 700 °C. This could imply either that the permeance of all gases at 650 °C is lower than expected or that the permeance at 600 or 700 °C is unexpectedly higher, breaking the volcano-shape trend.

Being the affinity of N_2 to the membrane surface, as well as its interaction with the water adsorbed on the surface of the pores negligible, we conclude that the $\wp_{N_2}$ trend with T_{carb} solely depends on the changes introduced by the carbonization temperatures in the porous structure, both in terms of pore size distribution and porosity of the membranes. As a result, on one hand, the trend of $\wp_{N_2}$ with T_{carb} can be explained with the information already available on the pore size distribution of these membranes. On the other hand, the $\wp_{N_2}$ can be used to elucidate even more on the effect that the carbonization temperature has on the pore size distribution of the membranes. All the techniques used for measuring the pore size distribution have some limitations: 1) physisorption techniques measure also dead-end pores, which are not active for the permeation, 2) perm-porometry techniques are based on capillary condensation phenomena, which requires strong hypothesis, especially for pore diameter below 1 nm. Therefore, we believe that using the permeation flux of inert species through the membrane is an effective way to have an indication of the properties of the porous system which are relevant for the permeation.

For this scope, it would be ideal to use, as a reference, the smallest inert gas of the system, which would have the possibility to access even smaller pores. In the previous section, we stated that H_2 does not interact with the membrane surface as its adsorption capacity measured via thermogravimetric analysis is negligible. Indeed, $\wp_{H_2}$ displays the exact same trend of $\wp_{N_2}$ vs T_{carb}, as well as of $\wp_{CO}$, which was also proved to be inert with respect to the membrane surface. As a result, each of these gases could be used to gain insights into the pore size distribution of the membranes.

Combining the information on the pore size distribution measured on unsupported carbon films from previous study and the trend reported in Fig. 11a, we can say that initially, $\wp_{N_2}$ increases with T_{carb} due to an increase in the porosity of the membranes and to the gradual development of pores in the MS region. At intermediate T_{carb} (600–700 °C), $\wp_{N_2}$

is the highest due to the large fraction of pores, especially in the MS region. At 650 °C, the $\wp_{N_2}$ is slightly lower, which could indicate that the membrane could also display some differences in terms of pore size distribution (i.e., a lower porosity or a shift in the average pore size to lower values). Finally, as soon as the porous structure starts to shrink (750 °C) also the $\wp_{N_2}$ decreases.

As it was shown in the previous section, these species do not adsorb on the membrane pores, thus molecular sieving is the dominant transport mechanism. At all carbonization temperatures, their permeance monotonically increases with the operating temperature, as reported in Fig. 12a for the membrane carbonized at 550 °C. This observation makes even clearer that, when the membranes display a high portion of pores in the MS region (i.e., T_{carb} in the range 600–700 °C), the gas permeance is also the highest.

The permeance of all species with a proved (i.e., water and CO_2) or expected (methanol) affinity to the membrane surface, is reported in Fig. 11b as a function of the carbonization temperature. Surprisingly, $\wp_{H_2O}$, $\wp_{CO_2}$ and $\wp_{MeOH}$ shows the same trend with T_{carb} as for the inert gases. However, Fig. 12b shows that $\wp_{H_2O}$ and $\wp_{MeOH}$ monotonically decrease when the operating temperature decreases, which is a clear indication of the adsorption diffusion being the dominant transport mechanism, as it was found in our previous study. Capillary condensation could also play a role, especially at lower temperatures. However, when using the information of the pore size distribution to estimate the capillary condensation pressure, we conclude that this phenomenon could play a role only at 150 °C (details on the calculations are given in S.I.).

CO_2 permeance ($\wp_{CO_2}$), instead, displays an optimum at ca. 200 °C, which is also typical of adsorption diffusion [61]. Indeed, since CO_2 permeance was measured through a humid membrane, some water molecules are adsorbed on the pore walls. This results in a reduced accessibility for the CO_2 to its adsorption sites, as well as in a lower active pore size, which make molecular sieving the dominant transport mechanism for $\wp_{CO_2}$. Moreover, when water is adsorbed on the pore walls, CO_2 can interact with it via dipole-quadrupole interactions in the larger AD pores [62,63]. As temperature increases (i.e., above 200 °C), water progressively desorbs and adsorption diffusion becomes the dominant mechanism for $\wp_{CO_2}$ as well.

These observations lead to the conclusion that the trend induced in the permeance of each species by the carbonization temperature solely depends on the characteristics of the porous structure of the membranes. On the other hand, the trend of the permeance of each species as a function of the operating temperature is strongly influenced by the
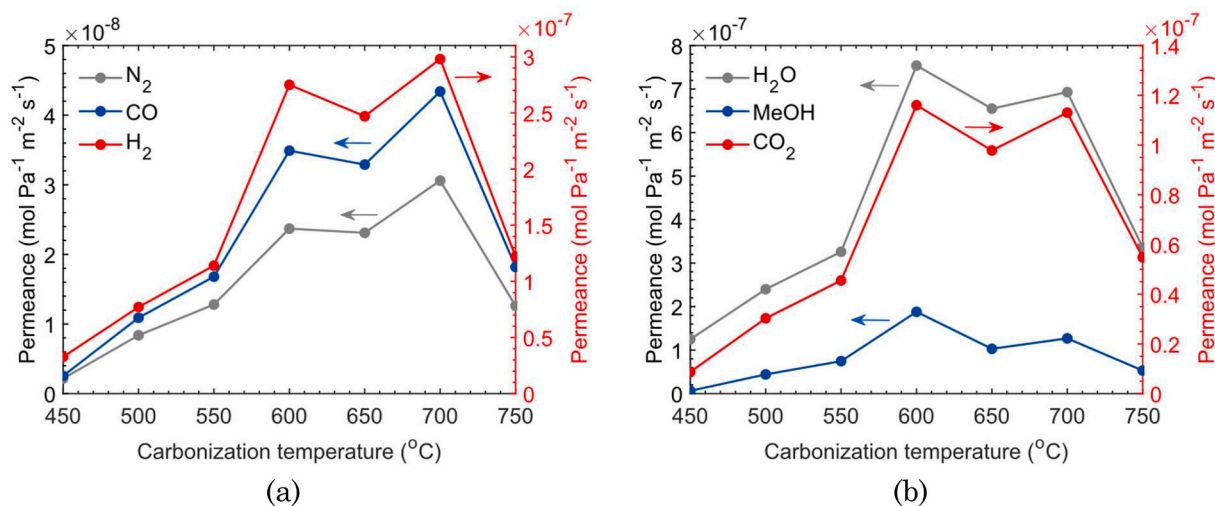

Fig. 11. Permeance of gases and vapors as a function of the carbonization temperature: (a) N_2, CO and H_2 (b) H_2O, methanol and CO_2, measured at 200 °C and a total pressure gradient of 3 bar.
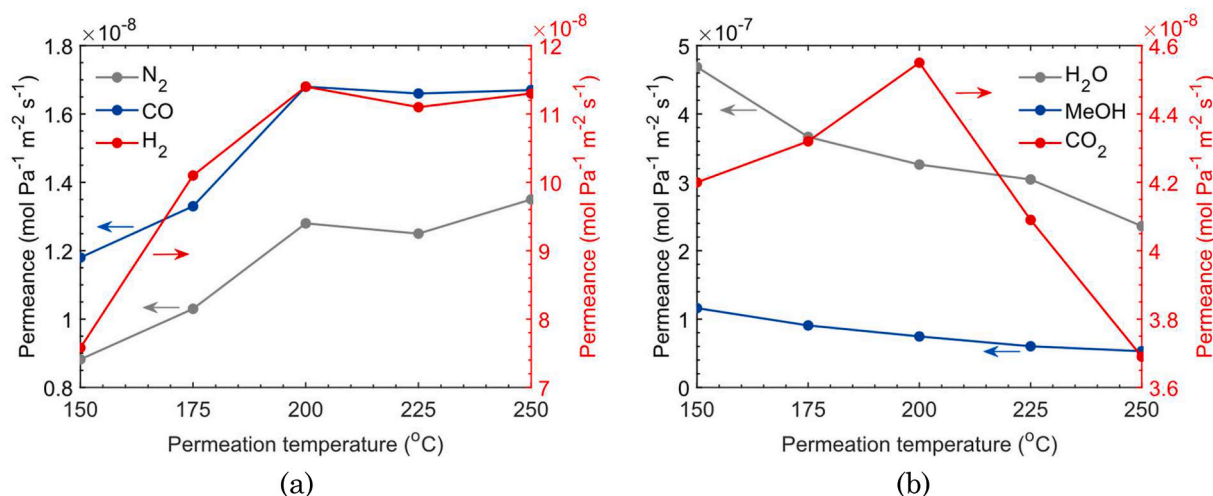
Fig. 12. Permeance of gases and vapors as a function of the permeation temperature: (a) N_2, CO and H_2 (b) H_2O, methanol and CO_2, measured at a total pressure gradient of 3 bar for the membrane carbonized at 550 °C.

dominant transport mechanism.

The trend of $\wp_i$ with the permeation temperature is qualitatively the same for all the membranes carbonized at different temperatures. However, as the permeation of water or methanol vapor are concern, the $\wp_{i,vapor}$ decrease with a different slope for different T_{carb}. In other words, the apparent activation energy (E_{act}^{app}) for both methanol and water (Fig. 13) is negative, which means that both species have a high adsorption energy ($E_{act}^{app} = E_{act,AD} - E_{ads} < 0$) and that adsorption diffusion is the dominant mechanism. However, when increasing the carbonization temperature, E_{act}^{app} increases, becoming less negative, assuming the highest value at ca. 600–700 °C, to then decrease again at 750 °C, thus showing a similar trend to the $\wp_i$ vs T_{carb} curves.

The only reason for the activation energy to increase is because of the interplay of two transport mechanisms, one being the adsorption diffusion, with a negative E_{act}^{app}, and the other molecular sieving, with a positive E_{act}^{app}. As a result, for the membranes carbonized in the range 600–700 °C, molecular sieving plays a relevant, although not dominant, contribution also in the permeation of water, methanol and CO_2. In conclusion, this is a further confirmation that MS pores appears gradually in the membrane porous structure and that a T_{carb} of 600–700 °C induces the formation of a large fraction of pores in the MS region, which subsequently shrinks for higher carbonization temperatures.
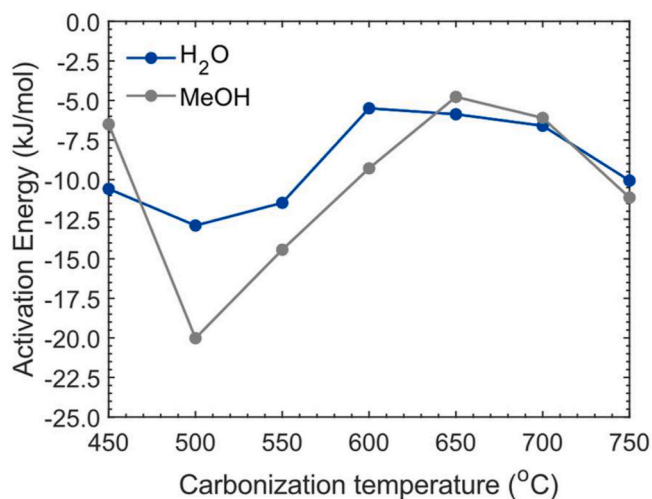

Fig. 13. Apparent activation energy as a function of the carbonization temperature for both methanol and water.

3.4.2. Insights into the gas permeation mechanism

In this section, the membrane carbonized at 600 °C is used as model to discuss the mechanisms involved in the permeation of the gases of interests, with a specific focus on how the presence of water affects the interplay of the transport phenomena.

Firstly, we observe that when $\wp_{H_2}$ (Fig. 14a) and $\wp_{CO}$ (Fig. 14b) are measured through a humid membrane and via a H_2/H_2O or CO/H_2O mixture, the permeance increases with the operating temperature with a similar slope, which indicates that molecular sieving is still dominant. However, both $\wp_{H_2}$ and $\wp_{CO}$ are higher when measured via pure gas permeation tests through a humid membrane. This indicates that when the gas/water mixture is fed to the membrane, water adsorbs on the pore walls, reducing the active pore size, thus partially or totally blocking some of the pores, hindering gas permeation.

On the other hand, when the membrane undergoes a thermal treatment which removes the adsorbed water from the surface, the pores will be bigger and the absence of water in the pores, makes the gases to collide with the walls of the pores increasing the path length behaving as Knudsen (microporous Knudsen) [64]. The Knudsen diffusivity depends on $T^{1/2}$, which means that the gas permeance decreases with temperature when Knudsen diffusion is the dominant mechanism. As a matter of fact, when $\wp_{H_2}$ and $\wp_{CO}$ are measured through a dry membrane we observe that $\wp_{H_2}$ slightly decreases with temperature, while $\wp_{CO}$ increases with temperature with a much lower slope than the previous cases. This means that when the membrane is dry, microporous Knudsen diffusion becomes the dominant transport mechanism for the H_2 permeation and it contributes to the permeation of CO, with molecular sieving being still dominant. Indeed, the mean free path of H_2 is larger than for CO, which explains the different contribution of the Knudsen flow for the two gases.

As we discussed in section 3.4.1, $\wp_{CO_2}$ is affected by both molecular sieving and adsorption diffusion. In Fig. 15, we observe that when water is adsorbed on the membrane pores (i.e., humid membrane) or it is fed together with CO_2 (i.e., mixture test), $\wp_{CO_2}$ displays an increase with the operating temperature, indicating molecular sieving as dominant mechanism. As a matter of fact, as we saw in Fig. 12, free water molecules reduce the accessibility of the adsorption sites for CO_2. As soon as this water is being removed from the pores, the pore size increases and adsorption diffusion becomes more relevant, to finally control the CO_2 transport when the membrane is dry. Indeed, $\wp_{CO_2}$ measured in dry conditions displays a negative activation energy, as clearly visible from Fig. 15. The decreasing trend of $\wp_{CO_2}$ with temperature recorded in dry conditions is not linked to the Knudsen diffusion. Indeed, the H_2O/CO_2
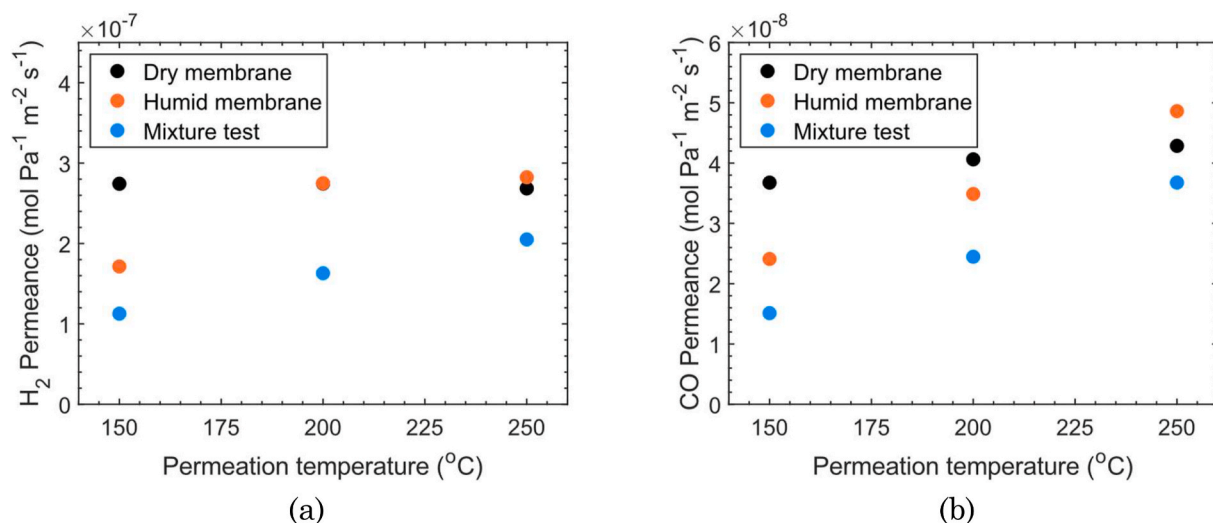
Fig. 14. H_2 permeance (a) and CO permeance (b) as a function of the permeation temperature measured through a dry and humid membrane and in gas/vapor mixtures for the membrane carbonized at 600 °C.

Fig. 15. CO_2 permeance as a function of the permeation temperature measured through a dry and humid membrane and in gas/vapor mixtures for the membrane carbonized at 600 °C.
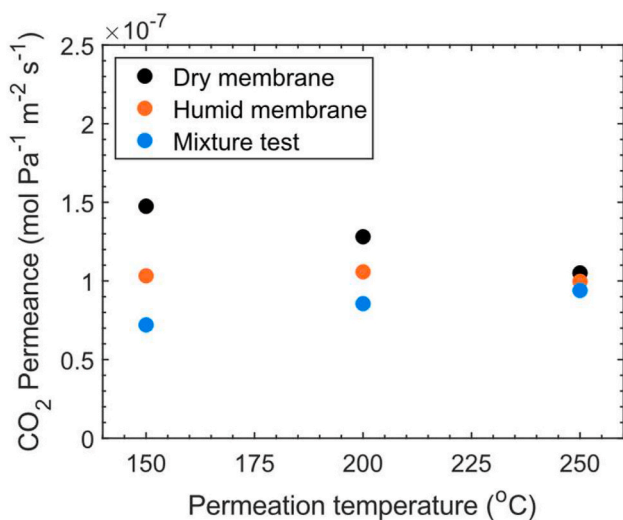
selectivity is 5.89 at 200 °C, which is ca. 4 times higher than the value of the Knudsen selectivity for the same gas/vapor pair (i.e., $\sqrt{Mw_{CO_2}/Mw_{H_2O}} = 1.56$).

The same experiments were carried out also for the membranes carbonized at 450 and 700 °C (see results in S.I.), which belong to the low porosity region, as seen in previous sections. Overall, we confirm that, even when removing the water via the thermal treatment (i.e., dry membrane), the permeance of the gases display the same trend with the carbonization temperature as in Fig. 11. On the contrary, the presence/absence of water in the membrane pores affect the relative contribution of the transport mechanism, which results in a different behavior of the permeance with the operating temperature.

3.4.3. Effect of the carbonization temperature on the vapor/gas perm-selectivity

The ideal perm-selectivity of water towards each of the gases and methanol ($S_{H_2O/i}$) were determined using the $\wp_i$ obtained via pure gas (via humid membrane) and pure vapor permeation tests. The behavior of $S_{H_2O/i}$ with respect to the gases (i.e., H_2, CO_2, CO, N_2) confirms what

was found in our previous study: $S_{H_2O/i}$ generally increases with the kinetic size and decreases with the permeation temperature for the gas showing molecular sieving behavior (i.e., H_2,CO and N_2). S_{H_2O/CO_2}, instead, is barely affected by the operating temperature, given the contribution of the adsorption diffusion in both CO_2 and water permeation mechanism.

Expectedly, all the perm-selectivity display the same trend as a function of T_{carb}, as for the $\wp_i$. As example, Fig. 16 depicts the S_{H_2O/H_2} vs T_{carb} measured in the temperature range 150–250 °C. At all operating temperatures, S_{H_2O/H_2} assumes the lowest values for the most permeable membranes (i.e., 600–700 °C). As a matter of fact, in membrane technology it is well known that a trade-off always exists between permeability and perm-selectivity, for a given separation. However, the trend is more marked at lower permeation temperatures (i.e., 150–175 °C), where capillary condensation phenomenon is more likely to contribute to the water permeation mechanism. This results in a higher probability for the water to partially or totally block some of the membrane hydrophilic pores, hindering the permeation of other gases. At 250 °C, the carbonization temperature barely affects the perm-selectivity.

The water/methanol perm-selectivity $S_{H_2O/MeOH}$ is also an important parameter when the scope of the membrane is to enhance reaction performance such as for the synthesis of MeOH or dimethyl ether (DME).
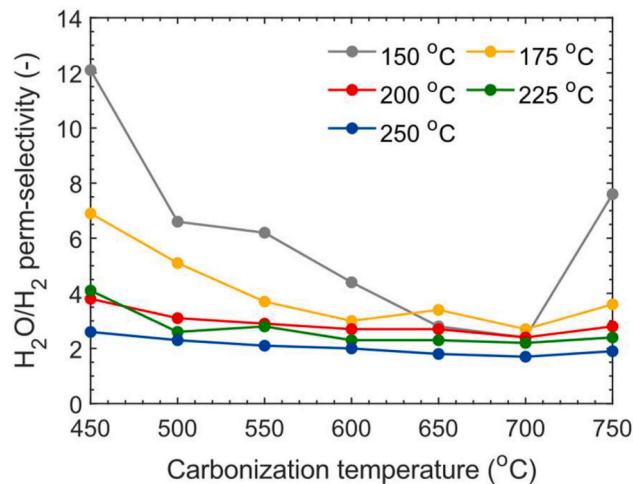

Fig. 16. H_2O/H_2 perm-selectivity as a function of the carbonization temperature measured at operating temperatures in the range 150–250 °C.

When methanol is the desired product, a low value of $S_{H_2O/MeOH}$ is preferred, in such a way that the equilibrium of the methanol synthesis is even more shifted to the products side. On the other hand, when methanol is the intermediate product, such as in the methanol to gasoline (MTG) process or in the DME synthesis, $S_{H_2O/MeOH}$ needs to be as high as possible, to keep the methanol in the reaction side. Fig. 17 displays the values of the $S_{H_2O/MeOH}$ determined for the membranes with different carbonization temperatures. $S_{H_2O/MeOH}$ displays the same trend with T_{carb} as seen for the water/gas pair. Furthermore, we observe that for most of the membranes, $S_{H_2O/MeOH}$ is not much affected by the operating temperature, given the very similar average dipolar moment (2.64 and 2.95 D for methanol and water, respectively) and activation energy of water and methanol. $S_{H_2O/MeOH}$ ranges from 3 to 6.4, except for the membrane carbonized at 450 °C which shows a selectivity of 19.9–16.5. Indeed, at T_{carb} of 450 °C, the membrane combines a high hydrophilicity with a relatively low porosity, which results in a much higher permeance of the water than of methanol.

Finally, when the permeation properties are measured feeding a mixture of gas and vapor, $\wp_{H_2O}$ decreases with a similar extent to what we observed for the gas permeance in Fig. 14 and in Fig. 15. When molecular sieving is the primary mechanism, the presence of water within the pores decreases the active pore size, leading to lower gas permeance. Conversely, when adsorption diffusion dominates, as with $\wp_{H_2O}$, the gradient in partial pressure positively affects permeance, as previously shown in our research [41]. Therefore, in the event of exposure to a vapor/gas mixture, the partial pressure of water is generally lower in both the retentate and permeate side of the membrane, resulting in a lower $\wp_{H_2O}$.

In conclusion, the separation is not significantly affected by the gas/vapor interactions, which means that the molecules need to compete for their transport through the membrane pores, despite the high affinity of the membrane to the water. This suggests that the competition between water and a second species occurs prior to the access of any molecule to the pores. Then, once water enters the pores, its transport is influenced by the interaction with the hydrophilic surface.

3.5. Membrane performance under reactive conditions

The results obtained under reactive conditions indicates that the packed bed membrane reactor (PBMR) technology leads to significant improvements in both methanol and DME synthesis compared to a packed bed reactor (PBR) tested under the same conditions (Fig. 18a and **b**). In particular, the integration of the carbon membrane for in-situ water removal leads to a notable 70% increase in methanol yield and

a 67% increase in DME yield. Such improvements confirm the predictions we obtained via our previous modeling studies [15,65], and highlight the relevance of this work. Indeed, the understanding of the relationship between surface functionality, intrinsic membrane properties, and vapor/gas separation performance is crucial and preparatory for the optimization of the membrane for a specific application.

To date, CMSMs have not been tested under reactive conditions for this particular reaction systems. Therefore, the study we proposed here is a crucial step towards demonstrating the efficacy of membrane reactor technology. It is pertinent to note that these results serve as a proof-of-concept, as further comprehensive elucidations concerning experimental procedures and outcomes are provided in a separate publication [52].

4. Conclusions

In this study, we prepared boehmite-phenolic resin carbon molecular sieve membranes, based on a previously optimized composition, carbonizing the membranes in the temperature range 450–750 °C. Both supported and unsupported membranes were tested to assess how the carbonization temperature affects the vapor-gas separation performance, in view of their potential application in membrane reactors, to enhance CO_2 hydrogenation reactions.

First, via FTIR analysis we elucidated on the transformation occurring in terms of the surface chemistry of the membranes as soon as the pyrolysis step progresses. We found that the OH groups disappear at $T_{carb} \geq 600$ °C. At the same temperature, the membrane also loses the aliphatic CH groups. The aromaticity, instead, disappear at higher temperature (700–750 °C), with the resin gradually transforming into a char-like structure.

The hydrophilicity of the membranes was first assessed via in-situ FTIR analysis, carried out when exposing the membrane to water vapor at ambient conditions. We found that two types of water adsorb onto the membrane surface: one directly bonded to the hydrophilic pores via H-bonds and the other free or weakly bonded, mostly interacting with the already adsorbed water (i.e., water monolayer). The membrane affinity to water initially increases with T_{carb}, with the sample carbonized at 500 °C being the most hydrophilic. Then, hydrophilicity tendentially decreases as hydrophilic functional groups are being removed.

The results of the thermogravimetric analysis revealed that the membrane is inert with respect to H_2, CO and N_2. On the other hand, CO_2 adsorption cannot be neglected and the affinity of the membrane to CO_2 generally increases with T_{carb}, due to a combination of a higher surface area and the possible transformation of the amine group into a pyridine/pyridone structure, which display stronger affinity to CO_2.

The permeance of all gases and vapors tested shows the same behavior with the carbonization temperature: $\wp_i$ first increases, displaying an optimum in the region 600–700 °C – with a slightly lower value at 650 °C – to decrease again at 750 °C. This result suggests that the trend induced by T_{carb} solely depends on the pore size distribution and porosity of the membranes. Indeed, the membranes carbonized in the range 600–750 °C display a bi-modal pore size distribution, with the majority of the pores in the MS region, which was confirmed also by the higher activation energy calculated for water and methanol.

On the other hand, the trend of $\wp_i$ with the operating temperature is strongly influenced by the transport mechanisms. Water, methanol and CO_2 permeate mostly via adsorption diffusion mechanism. The inert gases (i.e., H_2, CO and N_2), instead, permeates mostly via molecular sieving. However, when the permeance of such gases is measured through a dry membrane, microporous Knudsen diffusion starts to play a relevant role. Therefore, the presence/absence of water in the membrane pores affect the relative contribution of the transport mechanism, as well as the extent of the permeation flux: $\wp_i$ decreases for higher water content. Furthermore, when the permeance is measured via gas/vapor mixture, also the $\wp_{H_2O}$ decreases, indicating that all molecules,
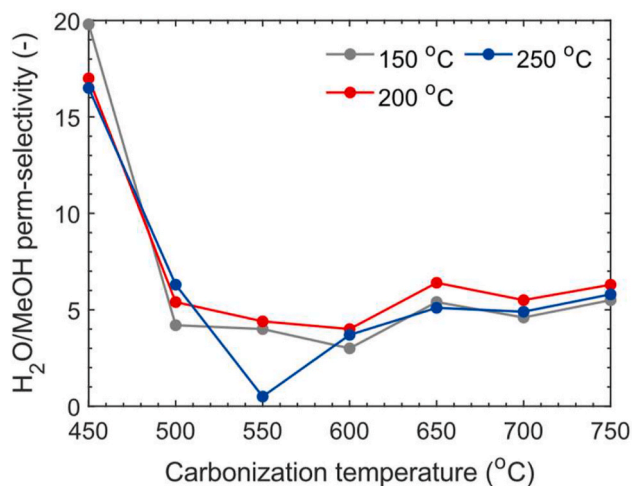

Fig. 17. Water/methanol perm-selectivity for the membranes carbonized at different temperatures, measured at 150, 200 and 250 °C.
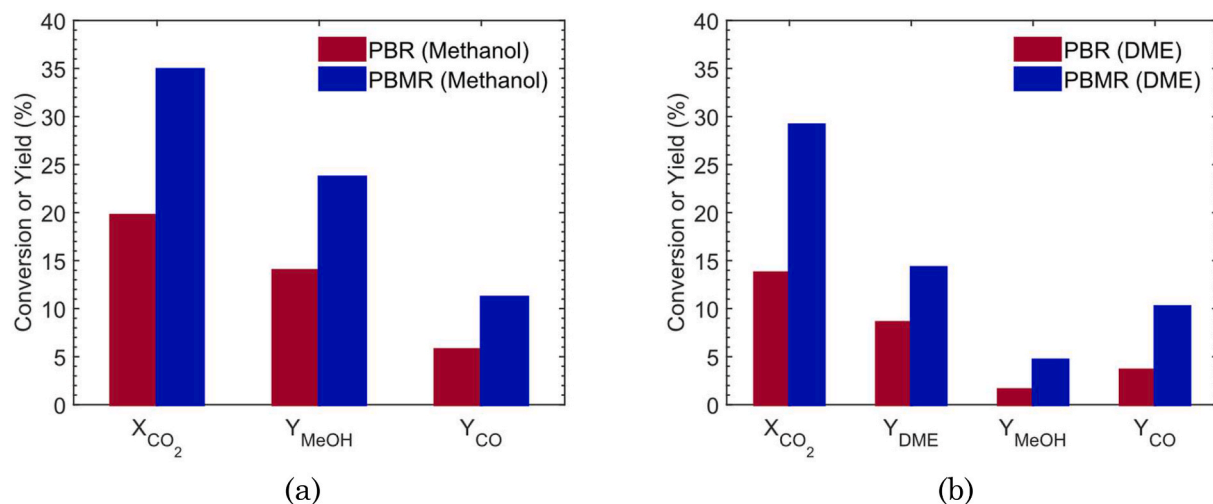
(a)   (b)

Fig. 18. CO_2 conversion and product yield obtained for the methanol (a) and DME synthesis (b) in a packed bed reactor (PBR) and in a packed bed membrane reactor (PBMR), based on the use of CMSM. Experimental conditions: reaction zone pressure (P^R) of 40 bar, $T = 200\ °C$, gas hourly space velocity (GHSV) of 400 $NL\ kg_{cat}^{-1}h^{-1}$ and a feed composition of $H_2/CO_2 = 3$; a pressure gradient across the membrane (ΔP) of 0 bar and a sweep gas ratio (SW) of 5 were used for the PBMR.

despites their affinity to the membrane surface, compete for accessing and interacting with the pores of the membranes.

Additionally, we observed that all the perm-selectivity display the same trend as a function of T_{carb}, as for the $\wp_i$, with the lowest values in the region 600–700 °C, corresponding to the highest permeabilities. This trend is more visible at low operating temperatures (i.e., 150–175 °C), where water condensation is more likely to occur and block some of the pores.

Finally, we experimentally proved that the integration of CMSMs in a packed bed reactor to promote the in-situ removal of water has great potential to enhance the CO_2 conversion to both methanol and DME, resulting in a notable improvement in the product yield of approximately 70%.

Author statement

S. Poto: Conceptualization; Data curation; Formal analysis; Investigation; Methodology Writing - original draft;

A. Aguirre, F. Huigh, Margot Anabell Llosa-Tanco, David Alfredo Pacheco-Tanaka, M. Fernanda Neira d'Angelo: Formal analysis;

Investigation; Methodology; Writing - review & editing.

Fausto Gallucci, Conceptualization; Funding acquisition; Project administration; Supervision; Writing - review & editing.

Declaration of competing interest

The authors declare that they have no known competing financial interests or personal relationships that could have appeared to influence the work reported in this paper.

Data availability

Data will be made available on request.

Appendix A. Supplementary data

Supplementary data to this article can be found online at https://doi.org/10.1016/j.memsci.2023.121613.

References

[1] J. Ma, et al., A short review of catalysis for CO2 conversion, Catal. Today 148 (3–4) (2009) 221–231.

[2] D. Chery, V. Lair, M. Cassir, Overview on CO 2 valorization: challenge of molten carbonates, Front. Energy Res. 3 (OCT) (2015) 1–10.

[3] J. Liu, K. Li, Y. Song, C. Song, X. Guo, Selective hydrogenation of CO2to hydrocarbons: effects of Fe3O4Particle size on reduction, carburization, and catalytic performance, Energy Fuel. 35 (13) (2021) 10703–10709.

[4] K.P. Kuhl, T. Hatsukade, E.R. Cave, D.N. Abram, J. Kibsgaard, T.F. Jaramillo, Electrocatalytic conversion of carbon dioxide to methane and methanol on transition metal surfaces, J. Am. Chem. Soc. 136 (40) (2014) 14107–14113.

[5] T.A. Atsbha, T. Yoon, P. Seongho, C.J. Lee, A review on the catalytic conversion of CO2using H2for synthesis of CO, methanol, and hydrocarbons, J. CO2 Util. 44 (2021). December 2020.

[6] S. Roy, A. Cherevotan, S.C. Peter, Thermochemical CO2 hydrogenation to single carbon products: scientific and technological challenges, ACS Energy Lett. 3 (8) (2018) 1938–1966.

[7] A. Álvarez, et al., Challenges in the greener production of formates/formic acid, methanol, and DME by heterogeneously catalyzed CO2 hydrogenation processes, Chem. Rev. 117 (14) (2017) 9804–9838.

[8] I. Iliuta, F. Larachi, P. Fongarland, Dimethyl ether synthesis with in situ H2o removal in fixed-bed membrane reactor: model and simulations, Ind. Eng. Chem. Res. 49 (15) (2010) 6870–6877.

[9] N. Diban, A.M. Urtiaga, I. Ortiz, J. Erenãa, J. Bilbao, A.T. Aguayo, Improved performance of a PBM reactor for simultaneous CO2 capture and DME synthesis, Ind. Eng. Chem. Res. 53 (50) (2014) 19479–19487.

[10] M. De Falco, M. Capocelli, A. Basile, C.B. Roma, ScienceDirect Selective membrane application for the industrial one-step DME production process fed by CO 2 rich streams : modeling and simulation, Int. J. Hydrogen Energy 42 (10) (2017) 6771–6786.

[11] N. Diban, A.M. Urtiaga, I. Ortiz, J. Ereña, J. Bilbao, A.T. Aguayo, Influence of the membrane properties on the catalytic production of dimethyl ether with in situ water removal for the successful capture of co 2, Chem. Eng. J. 234 (2013) 140–148.

[12] M. Farsi, A. Hallaji Sani, P. Riasatian, Modeling and operability of DME production from syngas in a dual membrane reactor, Chem. Eng. Res. Des. 112 (2016) 190–198.

[13] P. Rodriguez-Vega, et al., Experimental implementation of a catalytic membrane reactor for the direct synthesis of DME from H2+CO/CO2, Chem. Eng. Sci. 234 (2021).

[14] A. Ateka, J. Ereña, J. Bilbao, A.T. Aguayo, Strategies for the intensification of CO2 valorization in the one-step dimethyl ether synthesis process, Ind. Eng. Chem. Res. 59 (2) (2020) 713–722.

[15] S. Poto, F. Gallucci, M.F. Neira, Direct conversion of CO 2 to dimethyl ether in a fixed bed membrane reactor : influence of membrane properties and process conditions, Fuel 302 (February) (2021) 121080.

[16] M.S. Salehi, M. Askarishahi, F. Gallucci, H.R. Godini, Selective CO2-Hydrogenation using a membrane reactor, Chem. Eng. Process. - Process Intensif. 160 (2021), 108264. December 2020.

[17] F. Gallucci, A. Basile, A theoretical analysis of methanol synthesis from CO2 and H2 in a ceramic membrane reactor, Int. J. Hydrogen Energy 32 (18) (2007) 5050–5058.

[18] Y. Wen, J. Yuan, X. Ma, S. Wang, Y. Liu, Polymeric nanocomposite membranes for water treatment: a review, Environ. Chem. Lett. 17 (4) (2019) 1539–1551.

[19] N. Diban, A.T. Aguayo, J. Bilbao, A. Urtiaga, I. Ortiz, Membrane reactors for in situ water removal: a review of applications, Ind. Eng. Chem. Res. 52 (31) (2013) 10342–10354.

[20] A. Ateka, P. Rodriguez-Vega, T. Cordero-Lanzac, J. Bilbao, A.T. Aguayo, Model validation of a packed bed LTA membrane reactor for the direct synthesis of DME from CO/CO2, Chem. Eng. J. 408 (2021). October 2020.

[21] J. Gorbe, et al., Preliminary study on the feasibility of using a zeolite A membrane in a membrane reactor for methanol production, Sep. Purif. Technol. 200 (2018) 164–168. December 2017.

[22] F. Gallucci, Inorganic Membrane Reactors for Methanol Synthesis, Elsevier B.V., 2018.

[23] J. Hedlund, F. Jareman, A.J. Bons, M. Anthonis, A masking technique for high quality MFI membranes, J. Membr. Sci. 222 (1–2) (2003) 163–179.

[24] R. Lai, G.R. Gavalas, Surface seeding in ZSM-5 membrane preparation, Ind. Eng. Chem. Res. 37 (11) (1998) 4275–4283.

[25] R.M. Ravenelle, et al., Stability of zeolites in hot liquid water, J. Phys. Chem. C 114 (46) (2010) 19582–19595.

[26] J.B.S. Hamm, A. Ambrosi, J.G. Griebeler, N.R. Marcilio, I.C. Tessaro, L.D. Pollo, Recent advances in the development of supported carbon membranes for gas separation, Int. J. Hydrogen Energy 42 (39) (2017) 24830–24845.

[27] A.F. Ismail, L.I.B. David, A review on the latest development of carbon membranes for gas separation, J. Membr. Sci. 193 (1) (2001) 1–18.

[28] M. Kiyono, P.J. Williams, W.J. Koros, Effect of pyrolysis atmosphere on separation performance of carbon molecular sieve membranes, J. Membr. Sci. 359 (1–2) (2010) 2–10.

[29] W. Wei, G. Qin, H. Hu, L. You, G. Chen, Preparation of supported carbon molecular sieve membrane from novolac phenol-formaldehyde resin, J. Membr. Sci. 303 (1–2) (2007) 80–85.

[30] T.A. Centeno, A.B. Fuertes, Carbon molecular sieve membranes derived from a phenolic resin supported on porous ceramic tubes, Sep. Purif. Technol. 25 (1–3) (2001) 379–384.

[31] X. He, J. Arvid Lie, E. Sheridan, M.B. Hägg, CO2 capture by hollow fibre carbon membranes: experiments and process simulations, Energy Proc. 1 (1) (2009) 261–268.

[32] A.B. Fuertes, I. Menendez, Separation of hydrocarbon gas mixtures using phenolic resin-based carbon membranes, Sep. Purif. Technol. 28 (1) (2002) 29–41.

[33] N. Tanihara, H. Shimazaki, Y. Hirayama, S. Nakanishi, T. Yoshinaga, Y. Kusuki, Gas permeation properties of asymmetric carbon hollow fiber membranes prepared from asymmetric polyimide hollow fiber, J. Membr. Sci. 160 (2) (1999) 179–186.

[34] A.B. Fuertes, Adsorption-selective carbon membrane for gas separation, J. Membr. Sci. 177 (1–2) (2000) 9–16.

[35] Gas carbon, Sci. Am. 10 (47) (1855), 373–373.

[36] M.A. Llosa Tanco, J.A. Medrano, V. Cechetto, F. Gallucci, D.A. Pacheco Tanaka, Hydrogen permeation studies of composite supported alumina-carbon molecular sieves membranes: separation of diluted hydrogen from mixtures with methane, Int. J. Hydrogen Energy xxxx (2020).

[37] M.B. Rao, S. Sircar, Nanoporous carbon membrane for gas separation, Gas Sep. Purif. 7 (4) (1993) 279–284.

[38] S. Lagorsse, F.D. Magalhães, A. Mendes, Aging study of carbon molecular sieve membranes, J. Membr. Sci. 310 (1–2) (2008) 494–502.

[39] A. Rahimalimamaghani, D.A. Pacheco Tanaka, M.A. Llosa Tanco, F. Neira D'Angelo, F. Gallucci, New hydrophilic carbon molecular sieve membranes for bioethanol dehydration via pervaporation, Chem. Eng. J. 435 (P1) (2022), 134891.

[40] S. Tanaka, T. Yasuda, Y. Katayama, Y. Miyake, Pervaporation dehydration performance of microporous carbon membranes prepared from resorcinol/formaldehyde polymer, J. Membr. Sci. 379 (1–2) (2011) 52–59.

[41] S. Poto, J.G.H. Endepoel, M.A. Llosa-Tanco, D.A. Pacheco-Tanaka, F. Gallucci, M. F. Neira d'Angelo, Vapor/gas separation through carbon molecular sieve membranes: experimental and theoretical investigation, Int. J. Hydrogen Energy 47 (21) (2022) 11385–11401.

[42] C.W. Jones, W.J. Koros, Characterization of ultramicroporous carbon membranes with humidified feeds, Ind. Eng. Chem. Res. 34 (1) (1995) 158–163.

[43] A.B. Fuertes, D.M. Nevskaia, T.A. Centeno, Carbon composite membranes from Matrimid® and Kapton® polyimides for gas separation, Microporous Mesoporous Mater. 33 (1–3) (1999) 115–125.

[44] V.C. Geiszler, W.J. Koros, Effects of polyimide pyrolysis conditions on carbon molecular sieve membrane properties, Ind. Eng. Chem. Res. 35 (9) (1996) 2999–3003.

[45] M.A. Llosa Tanco, D.A. Pacheco Tanaka, A. Mendes, Composite-alumina-carbon molecular sieve membranes prepared from novolac resin and boehmite. Part II: effect of the carbonization temperature on the gas permeation properties, Int. J. Hydrogen Energy 40 (8) (2015) 3485–3496.

[46] L. Forster, et al., Tailoring pore structure and surface chemistry of microporous Alumina-Carbon Molecular Sieve Membranes (Al-CMSMs) by altering carbonization temperature for optimal gas separation performance: an investigation using low-field NMR relaxation measurements, Chem. Eng. J. (2021), 129313.

[47] M.A. Llosa Tanco, D.A. Pacheco Tanaka, S.C. Rodrigues, M. Texeira, A. Mendes, Composite-alumina-carbon molecular sieve membranes prepared from novolac resin and boehmite. Part I: preparation, characterization and gas permeation studies, Int. J. Hydrogen Energy 40 (16) (2015) 5653–5663.

[48] M. Teixeira, et al., Boehmite-phenolic resin carbon molecular sieve membranes-Permeation and adsorption studies, Chem. Eng. Res. Des. 92 (11) (2014) 2668–2680.

[49] M.L.V. Nordio, J.A. Medrano, M. Van Sint Annaland, D.A.P. Tanaka, M.L. Tanco, F. Gallucci, Water adsorption effect on carbon molecular sieve membranes in H2-CH4mixture at high pressure, Energies 13 (14) (2020).

[50] J.A. Medrano, M.A. Llosa-Tanco, D.A. Pacheco-Tanaka, F. Gallucci, Transport Mechanism and Modeling of Microporous Carbon Membranes, Elsevier Inc., 2019.

[51] S. Poto, D. Vico van Berkel, F. Gallucci, M. Fernanda Neira d'Angelo, Kinetic modelling of the methanol synthesis from CO2 and H2 over a CuO/CeO2/ZrO2 catalyst: the role of CO2 and CO hydrogenation, Chem. Eng. J. 435 (P2) (2022), 134946.

[52] S. Poto, M. A. Llosa-Tanco, D. A. Pacheco-Tanaka, F. Gallucci, and M. F. Neira d'Angelo, "Experimental investigation of a packed bed membrane reactor for the direct conversion of CO2 to Dimethyl Ether," J. CO2 Util., (Under review).

[53] C. Morterra, M.J.D. Low, I.R. studies of carbons - VII. The pyrolysis of a phenol-formaldehyde resin, Carbon N. Y. 23 (5) (1985) 525–530.

[54] C.J. Mitchell, G.R. Yang, J.J. Senkevich, Adhesion aspects of poly(p-xylylene) to SiO2 surfaces using γ-methacryloxypropyltrimethoxysilane as an adhesion promoter, J. Adhes. Sci. Technol. 20 (14) (2006) 1637–1647.

[55] H. Kumar, S.K. Tripathi, S. Mistry, G. Bajpai, Synthesis, characterization and application of coatings based on epoxy novolac and liquid rubber blend, E-J. Chem. 6 (4) (2009) 1253–1259.

[56] K.A. Trick, T.E. Saliba, Mechanisms of the pyrolysis of phenolic resin in a carbon/phenolic composite, Carbon N. Y. 33 (11) (1995) 1509–1515.

[57] L.J.F.C. Bellamy, The Infra-red Spectra of Complex Molecules, Springer Science & Business Media, 2013.

[58] L. Forster, et al., Tailoring pore structure and surface chemistry of microporous Alumina-Carbon Molecular Sieve Membranes (Al-CMSMs) by altering carbonization temperature for optimal gas separation performance : an investigation using low-field NMR relaxation measurements, Chem. Eng. J. 424 (2021), 129313. December 2020.

[59] Fourier Transform Infrared Spectroscopy Studies of Water Uptake in Chemically Amplified Photoresists", pp. 1–22.

[60] G. Lim, K.B. Lee, H.C. Ham, Effect of N-containing functional groups on CO2 adsorption of carbonaceous materials: a density functional theory approach, J. Phys. Chem. C 120 (15) (2016) 8087–8095.

[61] P.F. Lito, S.P. Cardoso, A.E. Rodrigues, C.M. Silva, Kinetic modeling of pure and multicomponent gas permeation through microporous membranes: diffusion mechanisms and influence of isotherm type, Separ. Purif. Rev. 44 (4) (2015) 283–307.

[62] B. Petrovic, M. Gorbounov, S.M. Soltani, Microporous and Mesoporous Materials Influence of surface modification on selective CO 2 adsorption : a technical review on mechanisms and methods, September 312 (2020) 2021.

[63] N. Chanut, S. Bourrelly, B. Kuchta, and C. Serre, "Screening the Effect of Water Vapour on Gas Adsorption Performance : Application to CO 2 Capture from Flue Gas in Metal – Organic Frameworks",.

[64] J. Gilron, A. Soffer, Knudsen Diffusion in Microporous Carbon Membranes with Molecular Sieving Character, vol. 209, 2002, pp. 339–352.

[65] S. Poto, T. Vink, P. Oliver, F. Gallucci, M.F. Neira D'Angelo, Techno-economic assessment of the one-step Co2 conversion to dimethyl ether in a membrane-assisted process, J. CO2 Util. 69 (2023) 102419.